MICROCOPY RESOLUTION TEST CHART

NATIONAL BUREAU OF STANDARDS-1963-A

AURORAL HIGH LATITUDE MORPHOLOGY AND DYNAMICS

S.-I. Akasofu

Geophysical Institute, University of Alaska
903 Koyukuk Avenue North
Fairbanks, Alaska 99701

Final Report
February 16, 1979 - June 16, 1982

September 16, 1982

DTIC
SELECTED
JAN 14 1983

83 01 14 003

REPORT DOCUMENTATION PAGE		READ INSTRUCTIONS BEFORE COMPLETING FORM
1. REPORT NUMBER AFGL-TR-82-0248	2. GOVT ACCESSION NO. AD-A??3???	3. RECIPIENT'S CATALOG NUMBER
4. TITLE *(and Subtitle)* AURORAL HIGH LATITUDE MORPHOLOGY AND DYNAMICS		5. TYPE OF REPORT & PERIOD COVERED Final Report 16 Feb 1979 - 16 June 1982
		6. PERFORMING ORG. REPORT NUMBER
7. AUTHOR(s) S. -I. Akasofu		8. CONTRACT OR GRANT NUMBER(s) F19628-79-C-0067
9. PERFORMING ORGANIZATION NAME AND ADDRESS Geophysical Institute, University of Alaska 903 Koyukuk Avenue North Fairbanks, Alaska 99701		10. PROGRAM ELEMENT, PROJECT, TASK AREA & WORK UNIT NUMBERS 62101F 464306AE
11. CONTROLLING OFFICE NAME AND ADDRESS Air Force Geophysics Laboratory Hanscom AFB, Massachusetts 01731 Monitor/James G. Moore/PHY		12. REPORT DATE 16 September 1982
		13. NUMBER OF PAGES 49
14. MONITORING AGENCY NAME & ADDRESS *(if different from Controlling Office)*		15. SECURITY CLASS. *(of this report)* Unclassified
		15a. DECLASSIFICATION/DOWNGRADING SCHEDULE

16. DISTRIBUTION STATEMENT *(of this Report)*

Approved for public release; distribution unlimited

17. DISTRIBUTION STATEMENT *(of the abstract entered in Block 20, if different from Report)*

18. SUPPLEMENTARY NOTES

19. KEY WORDS *(Continue on reverse side if necessary and identify by block number)*

Geomagnetic storm prediction scheme and modeling of the magnetosphere

20. ABSTRACT *(Continue on reverse side if necessary and identify by block number)*

We have established the outline of the geomagnetic storm prediction scheme for defense systems which are vulnerable to geomagnetic activity.

DD ${}_{1\ JAN\ 73}^{FORM}$ 1473   EDITION OF 1 NOV 65 IS OBSOLETE

Table of Contents

iii

A

General Summary

Geomagnetic storms arise from a large-scale electrical discharge process surrounding the earth and it has been known that they are one of the most serious natural hazards to the Defense Systems. One possible solution to this hazard is: (i) to forecast accurately the occurrence and intensity of geomagnetic storms, (ii) to alert all warning systems which would fail during geomagnetic storms, and (iii) to mobilize emergency systems to supplement them. Thus, the accuracy of forecasting the occurrence and intensity of geomagnetic storms is of utmost importance. Reliable forecasting would be able to reduce drastically expenses involved in mobilizing these emergency systems.

We have recently made important progress in the forecasting by the discovery of a particular solar wind parameter which controls the development of geomagnetic storms. This quantity ε is given by

$$\varepsilon = VB^2 \sin^4 \left(\frac{\theta}{2}\right) \ell_o^2$$

where

$\quad$ V = the solar wind speed

$\quad$ B = the solar wind magnetic field magnitude

$\quad$ θ = the polar angle of the solar wind magnetic field vector

$\quad$ ℓ_o = constant (≈ 7 earth radii)

Having this quantity, our tentative criterion for the defense systems which are vulnerable to geomagnetic activity may be given as follows:

$\quad$ $\varepsilon < 10^{18}$ erg/sec – normal operation

$\quad$ $\varepsilon \sim 5 \times 10^{18}$ erg/sec – require alert

$\quad$ $\varepsilon \sim 10^{19}$ erg/sec – prepare for system failure

$\quad$ $\varepsilon > 10^{20}$ erg/sec – system failure

Major Results

I. Establishment of the outline of the geomagnetic storm prediction scheme for the defense systems which are vulnerable to geomagnetic activity

Summary

Several recent major advances in solar-terrestrial physics have made the prediction of geomagnetic storms a definite possibility. The operation of defense systems which are vulnerable to geomagnetic activity can be greatly strengthened by a computer system which displays the predicted problem areas on a computer screen on a continuous basis with a 6-12 hour lead time. We have most of the major computer codes for our purpose, although some have to be improved to meet our specifications. Thus, one of our main efforts should be to assemble the codes for our particular purpose.

1. Introduction

It has become apparent that the implementation of a geomagnetic storm prediction scheme will significantly improve the capability of defense systems which are vulnerable to geomagnetic activity. Specifically, it is important to predict the location of the equatorward boundary of the auroral oval and characteristics of the ionospheric trough (such as the depth and width) with a 6-12 hour lead time on a continuous basis and display this information using a dynamic computer display system. Such a prediction scheme has become a definite possibility by several recent important advances in solar-terrestrial physics, including the finding of the solar wind-magnetosphere energy coupling function ε, the success of the first three-dimensional simulation of disturbed solar wind conditions caused by solar flares and the development of various

2

computer codes in modeling the ionosphere. In Sections IV and V, some of the details of the recent progress are reported.

Therefore, it is important to set up a practical <u>numerical</u> prediction scheme specifically for the defense systems which are vulnerable to geomagnetic activity. The scheme consists of a number of powerful computer codes. Inputs for the computer codes are various solar observations and earthbound satellite observations (as will be described below in detail), and the outputs are the equatorward boundary of the auroral oval and the trough conditions which are displayed on a dynamic display system. What is important at this point of the development of the storm prediction scheme is: (i) to identify all necessary computer codes, (ii) to develop missing codes; (iii) to assemble all the codes, (iv) to test and improve the scheme.

2. <u>General Prediction Scheme: Figure 1</u>

(1) <u>Input</u>

The input consists of: (i) coronal hole monitoring and (ii) solar flare monitoring.

(i) <u>Coronal hole monitoring</u>

The coronal hole can be monitored by

(a) The white light coronal observation at the eastern limb of the sun at the Sacramento Peak Observatory and elsewhere.

(b) The magnetic field survey on the photospheric level at the Kitt Peak and the Mt. Wilson Observatories.

(c) If available, satellite soft x-ray photographs of the sun (like Skylab photographs).

GEOMAGNETIC STORM PREDICTION SCHEME

Fig. 1

(ii) Solar flare monitoring

The existing network of solar flare patrol systems can provide the basic input data. A sudden disappearance of chromospheric filaments appears to be another (perhaps more important) source (or indication) of the occurrence of a high speed stream (Joselyn and McIntosh, 1981).

(2) Basic codes

(a) Basic solar wind code

The basic solar wind code (i) analyzes the input data (1) and determines the solar magnetic equator on a sphere of 2.5 solar radii (the source surface); (ii) infers the solar wind speed distribution on the source surface; and (iii) computes the expected solar wind speed V, density n, magnetic field magnitude B and orientation (θ, ϕ) at the location of the earth.

(b) ε computation code

The ε computation code takes the solar wind quantities (V, B, θ, ϕ) at the location of the earth as a function of time, computed by the basic solar wind code and computes the power $\varepsilon(t)$ generated by the solar wind-magnetosphere generator as a function of time.

(c) Auroral oval geometry code

The oval geometry code takes the power ε as the input and determines the geometry of the poleward boundary of the auroral oval in magnetic latitude – MLT coordinates. This code can predict also the equatorward boundary of the oval, along which the auroral E appears.

5

(d) <u>AE, Dst prediction code</u>

This code takes the power ε as the input and predicts the AE and Dst indices.

(e) <u>Magnetospheric convection code</u>

This code takes the power ε as the input and determines the convection pattern of magnetospheric plasma over the entire polar ionosphere. It has been determined empirically that the cross-polar cap poten' 'al is proportional to $\sqrt{\varepsilon}$ (Reiff et al., 1981). Combining this empirical re t with the auroral oval geometry code, one can infer the distribution of t electric field in the polar regions.

(f) <u>Empirical auroral oval-trough code</u>

This code provides the geometry of the oval and the trough for given AE and Dst values as the input data. The basis for this code is an empirical study of the relationship between the oval geometry and the AE, Dst indices. At the present time, the oval geometry can be provided graphically for a given Q index or AE index. This code is a backup to the auroral oval geometry code.

(g) <u>Ionospheric code</u>

This code determines the electron density profile of the F2 region as a function of latitude and MLT for a given magnetospheric convection flow condition on a given day by using the magnetospheric convection code as the input data (Watkins, 1978; Sojka et al., 1982).

(h) Energetic particle drift code

Since the mantle aurora is produced by energetic electrons which drift eastward in the morning sector, this code is needed in determining the location of the mantle aurora.

(i) Prediction of the equatorward boundary of the auroral oval and trough

The codes (c), (f) and (g) can be developed in such a way that their outputs, namely the equatorward boundary of the oval (of both discrete and diffuse auroras) and the ionospheric trough, are displayed on a computer display screen on a continuous basis.

(j) Flare-generated wind code

The scheme presented in the above provides the 'background' conditions of the solar wind and the auroral oval, etc. A solar flare introduces an additional disturbance to the background condition. The solar wind condition after a solar flare depends greatly on the solar wind condition prior to a flare (namely, the background condition) since the former results partly from the interaction between the slow background wind and the flare-generated fast wind.

The flare wind code takes (i) the observed location of the flare with respect to the solar magnetic equator, (ii) the central meridian distance; (iii) its time development; and (iv) the maximum intensity as the input data. These input data enable us to introduce "disturbance" into the background basic solar wind code, simulating numerically disturbed solar wind conditions. A sudden disappearance of chromospheric filaments appears to be another (perhaps more important) indication of the occurrence of a high speed

7

stream. However, it is necessary to quantify the observations in terms of (iii) and (iv).

II. Establishment of a practical geomagnetic storm prediction scheme

Summary

We have contributed in establishing a direct communication link between the ISEE/C satellite and the Geophysical Institute via the Space Environmental Laboratory, Boulder, Colorado in predicting geomagnetic storm activity. This direct link has been very useful for the operation of rocket launching at the Poker Flat Rocket Range. In fact, the system was operated for the first time in 1981 when Air Force rockets were launched.

During the last several years, we have emphasized the importance of monitoring this solar wind parameter on a real time basis by a satellite which is located at the front of the earth. Fortunately, the International Sun-Earth-Explorer C was placed at the libration point, about 1.6 million kilometers from the earth toward the sun, in the fall of 1978. From its location, the satellite monitors the solar wind and relays the data to ground tracking stations, then to the NASA Goddard Space Flight Center (Maryland), and to the NOAA Space Environmental Laboratory (Colorado) where the solar wind-magnetosphere energy coupling function ϵ is computed. As an experiment, the computed data were transmitted to the GEOS satellite over the Pacific Ocean and finally relayed to the Geophysical Institute during the spring rocket campaign in 1981. It takes about 60 minutes for the solar wind to reach the earth from the satellite location, while it takes only about 7 seconds for data transmission. Figure 2 shows schematically the communication link between the ISEE/C satellite and the Geophysical Institute. Figure
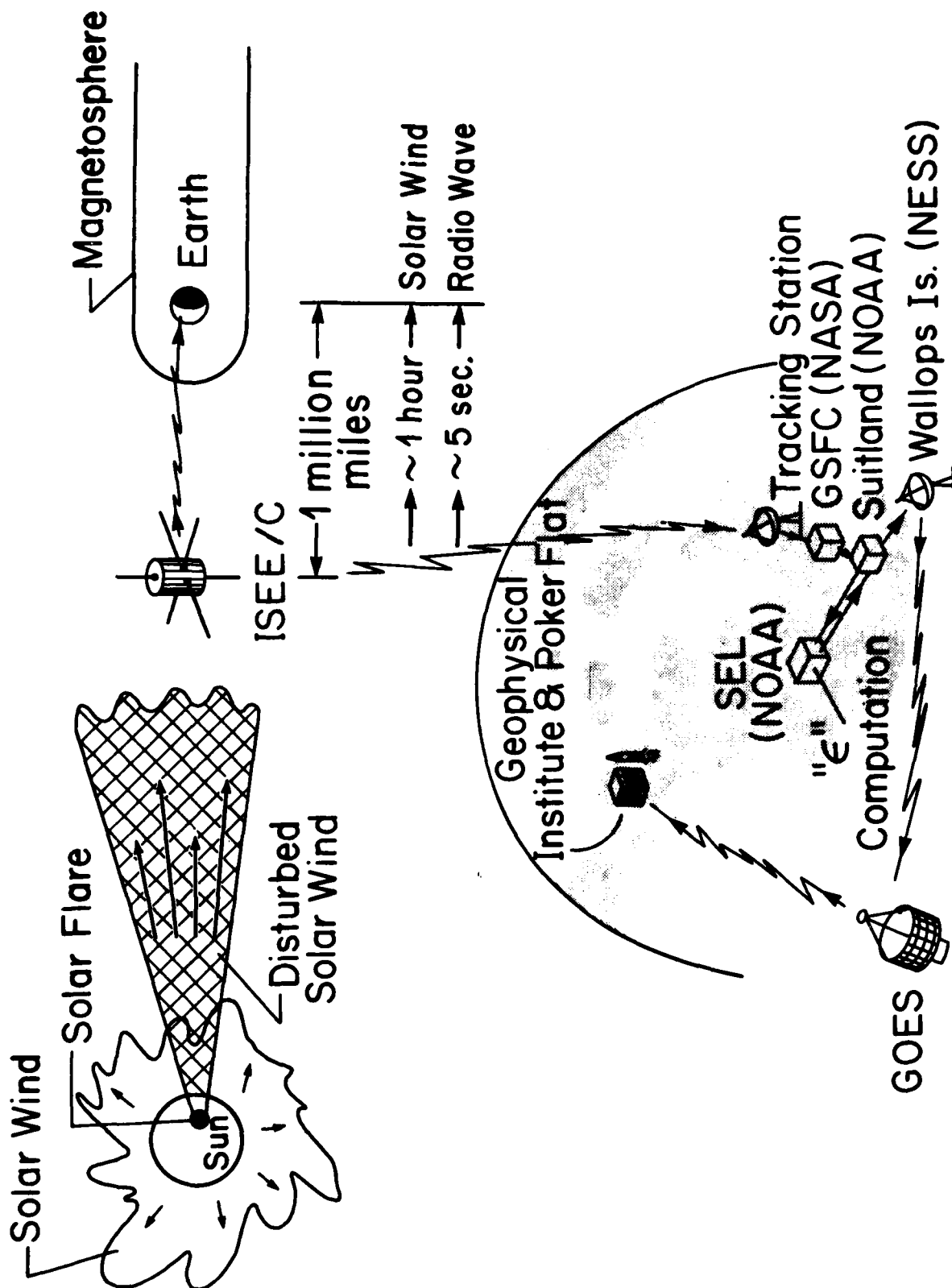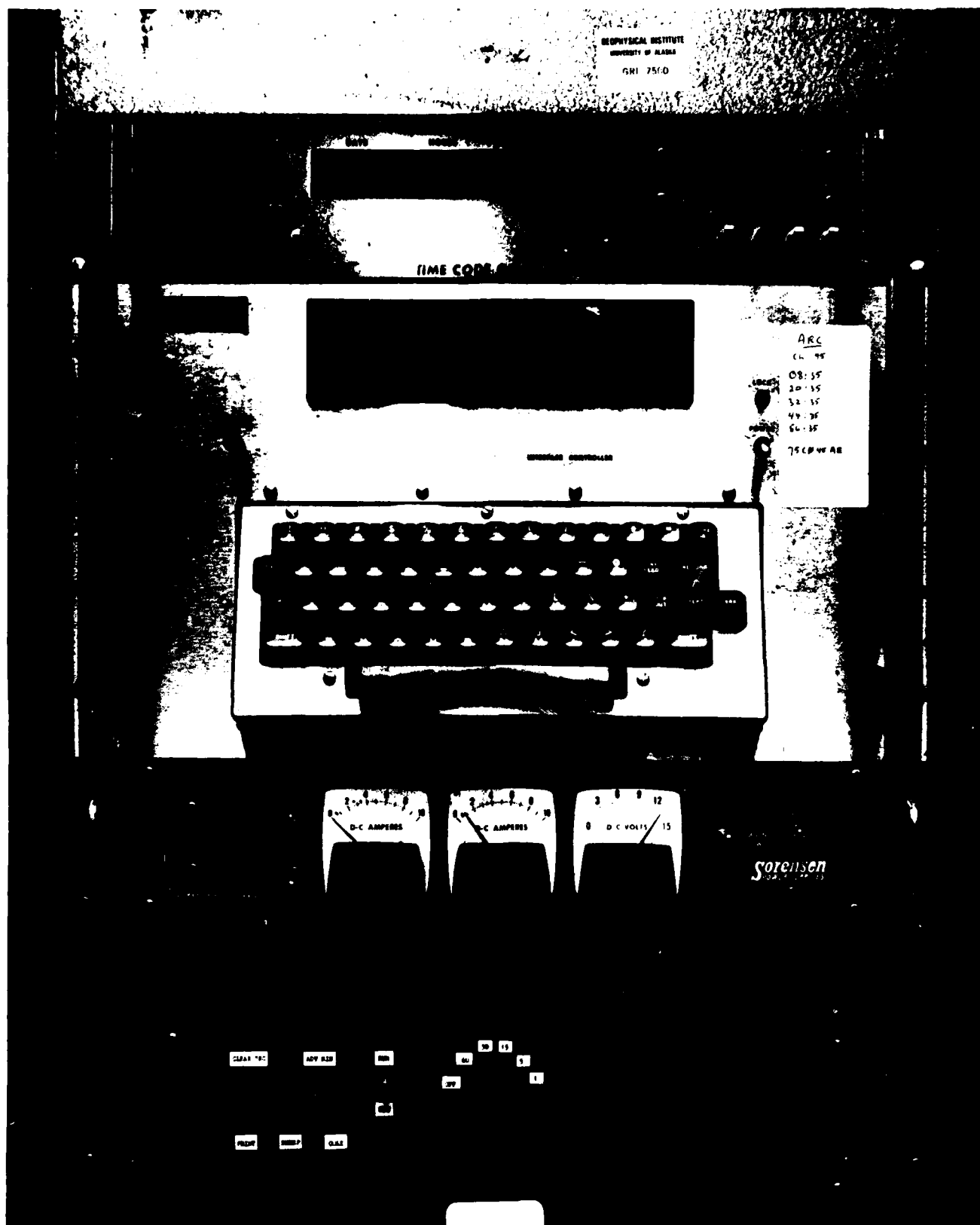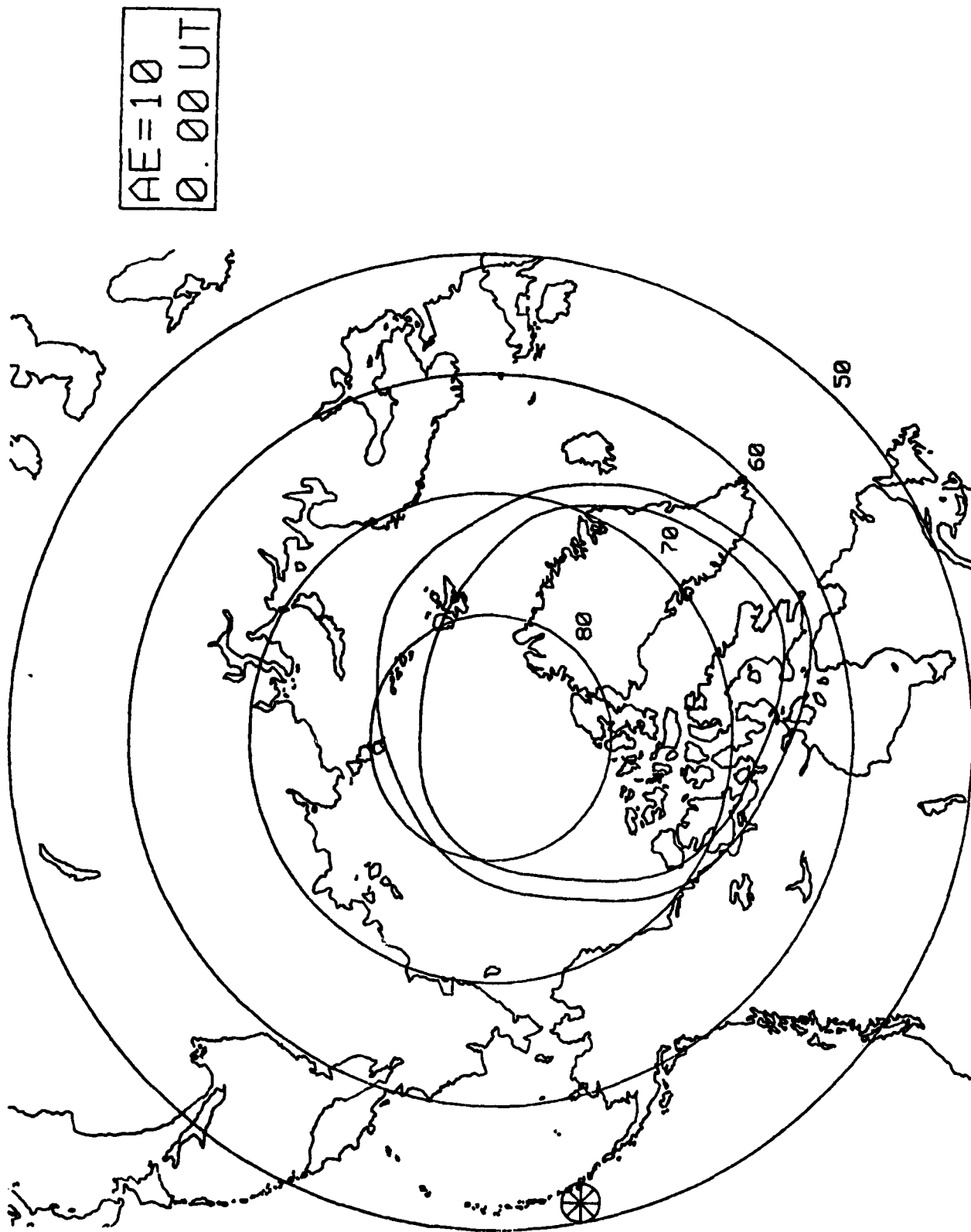
Fig. 2

Fig. 3

AE=10
0.00 UT

Fig. 4a
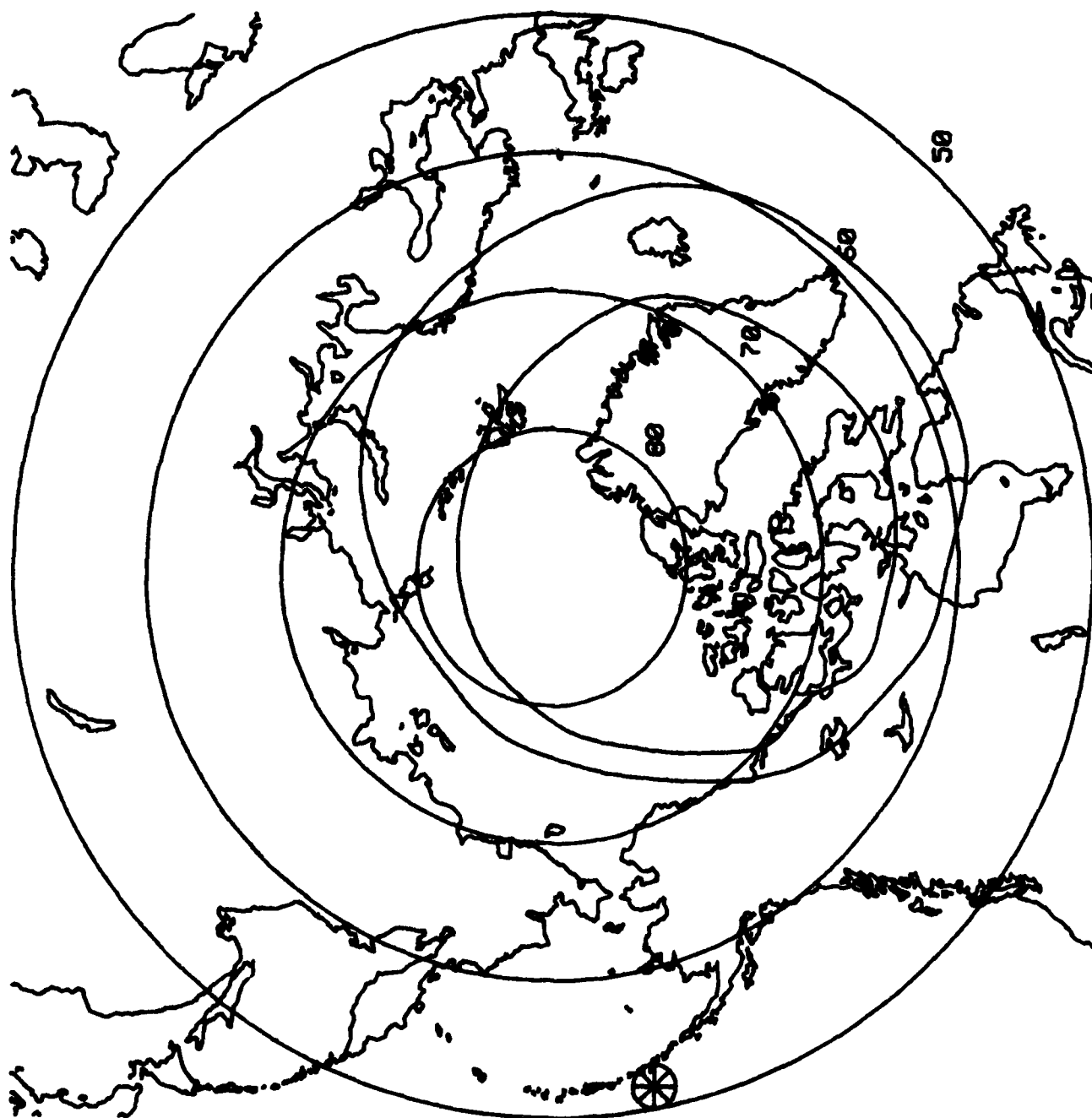
11

AE=140
0.00UT

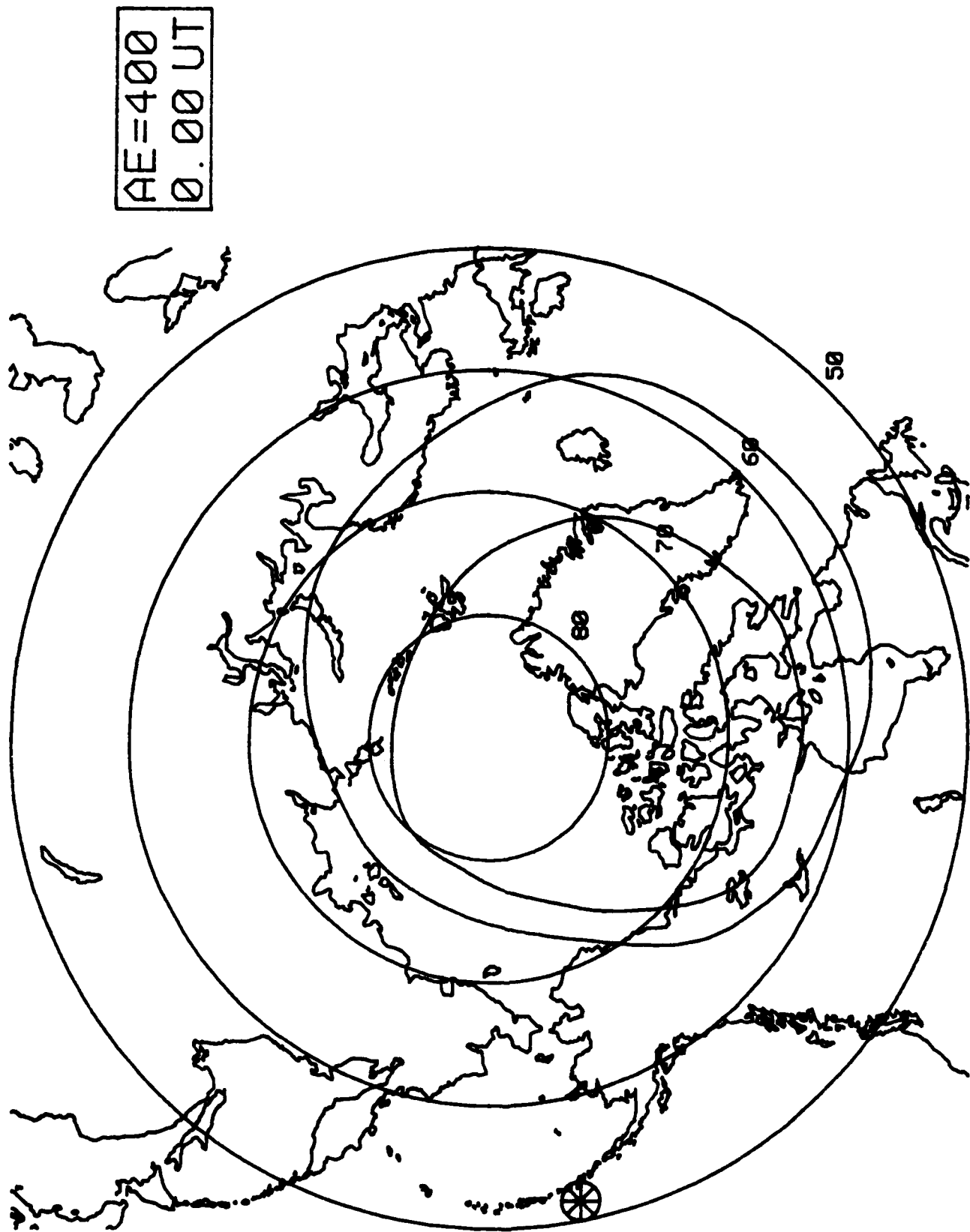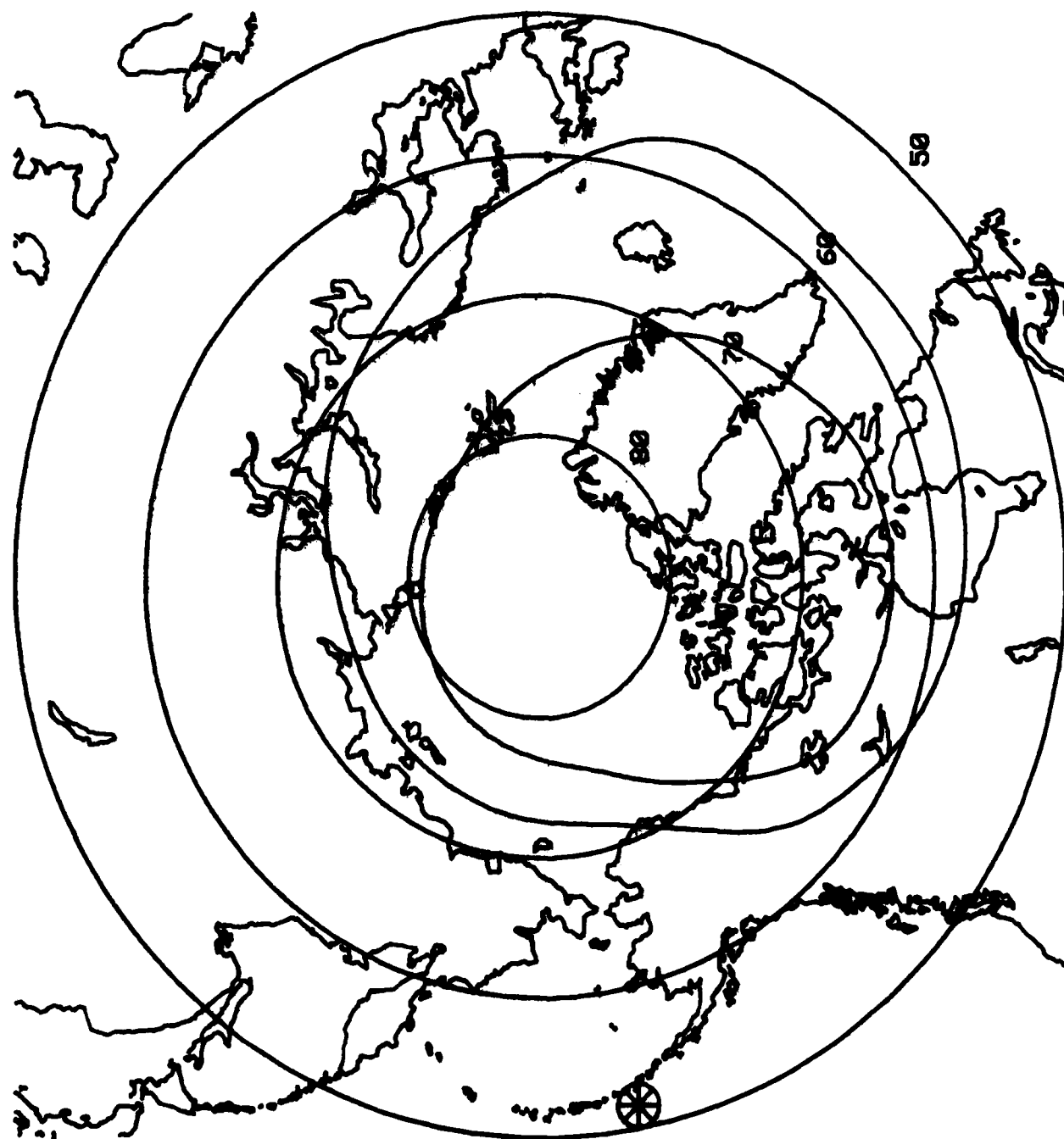Fig. 4b

12

AE=400
0.00 UT

Fig. 4c

13

AE=660
0.00 UT

Fig. 4d

14

3 shows our receiving instrument. Because of a limited communication capability, ε values are coded; 2×10^{18} = 2,8, 5×10^{19} = 5,9, 7×10^{17} = 7,7. The coded values were sent from Boulder every 5 minutes. When ε values were less than 10^{18}, auroras became quiet. When ε values exceeded 10^{19} for an extended period (~3 hrs), auroras remained in the southern sky, unsuitable for rocket launches. When ε values increased from very low values ($<10^{17}$ erg/sec) to 10^{18} erg/sec or greater, auroral activity increased significantly about 40 minutes afterwards. Thus, this experiment was quite successful and useful for rocket scientists, since they were able to schedule the launch of their rockets in time to intercept the forecasted auroral activity. The Global Weather Central, Offutt AFB is also monitoring ε on a real time basis by using solar wind quantities which are telemetered from the ISEE/C satellite at the libration point (located at a distance of 240 earth radii toward the sun).

III. <u>Computer display system of the auroral oval</u>

We set up a computer scheme to display the location of the auroral oval for a given Q at a given UT on a CRT with the polar geographic map. This is a computer version of the templet scheme constructed by Whalen (1970) "Auroral oval plotter and monograph for determining corrected geomagnetic local time, latitude, and longitude for high latitudes in the northern hemisphere." Figures 4a-d show some of the examples taken from the CRT for AE = 0γ, 140γ, 400γ and 660γ at 00 UT.

We have also constructed a model of the magnetosphere which depends on the interplanetary magnetic field (IMF). It is possible to determine the "open region" in the polar cap for the IMF of a given magnitude and orientation. Assuming that the boundary of the open region delineates approximately the auroral oval, we have devised a computer scheme to show the

15

open area on CRT. An important remaining task is to convert the Q index to the AE index.

IV. Prediction of the development of geomagnetic storms using the solar wind-magnetosphere energy coupling function ε

Summary

In this section, we explain how the Dst and AE prediction codes have been developed. In particular, it is shown that by monitoring time variations of the solar wind-magnetosphere energy coupling function ε(t) upstream of the solar wind, one should be able to predict fairly accurately the growth and decay of individual magnetospheric substorms and storms. In this section, we show how the two key geomagnetic storm indices, Dst and AE, can be estimated on the basis of the predicted values of ε. For details of this study, see Akasofu (1981, 1982)

1. Formulation

It is generally agreed that the major part of the energy transferred from the solar wind to the magnetosphere is deposited in the ring current, so that we assume that 70% of ε is consumed in the formation of the ring current belt, namely that the rate U_R of ring current particle injection is given by $U_R = 0.7\varepsilon$. The predicted ring current field DR(γ) is then obtained by integrating the equation

$$4 \times 10^{20} \left(\frac{\partial DR}{\partial t} + \frac{DR}{\tau_R} \right) - 0.7\varepsilon$$

where τ_R is the lifetime of the ring current particles. The dependence of τ_R

16

on storm intensity is taken to be:

$$\tau_R = 20 \text{ h for } \varepsilon < 10^{18} \text{ ergs}^{-1}$$

$$= 2\text{h for } 10^{18} \text{ ergs}^{-1} \varepsilon < 10^{19} \text{ ergs}^{-1}$$

$$= 1 \text{ h for } \varepsilon > 10^{19} \text{ ergs}^{-1}$$

As we shall see later, this set of values of τ_R tends to predict slightly greater main phase decreases than observed ones. However, we shall use this set in this paper, since a similar set has been used extensively in the past.

The Dst index consists of at least two components, the ring current field $DR(\gamma)$ and the solar wind compression field $DCF(\gamma)$. The solar wind compression field is given by

$$DCF(\gamma) = 13.1 \times 10^4 (\sqrt{p_2} - \sqrt{p_1})$$

where p_1 and p_2 denote the solar wind pressure before and after storm onset. Therefore, taking into account (2) and (3), the predicted Dst index (Dst_p) is given by

$$Dst_p = DCF - DR.$$

In the next section, the baseline of Dst_p is adjusted to give $Dst = Dst_p$ at the beginning of each storm period.

17

There is still much uncertainty between the Joule heat production rate U_J in the ionosphere and the AE index, although the rate U_J in the polar ionosphere is 10-30% of the power ϵ generated by the solar wind-magnetosphere dynamo. One of the complications involved in this particular study is that U_J is approximately proportional to ϵ for small values of ϵ ($<10^{19}$ ergs^{-1}), but this relation breaks down for $\epsilon > 10^{19}$ ergs^{-1}. Therefore, we use here an empirical relationship between ϵ and the AE index which includes the fact that the AE index tends to "saturate" for $\epsilon > 10^{19}$ ergs^{-1}. The empirical expression is given by

$$AE_p(\gamma) = -300 \ (log)^2 + 11,700 \ log \ \epsilon - 11,3200.$$

2. Examples

In this section, we study first one of the simplest storm developments in detail and then examine how well the solar wind-magnetosphere coupling function ϵ can predict the development of geomagnetic storms in terms of the predicted Dst index (Dst_p).

Figure 5 shows, from the top, the solar wind-magnetosphere energy coupling function ϵ, Dst_p, the observed Dst, AE_p and the observed AE index, for the 16-18 March, 1974 storm. No time delay is assumed in the energy coupling and dissipation processes.

Prior to the onset of the storm of March 16, 1974 (ssc at 1128 UT), there occurred minor substorm activity with $\epsilon \sim 2 \times 10^{18}$ ergs^{-1}, which caused a weak ring current, as indicated by a slight depression of the Dst index. This change is reproduced fairly well in the predicted Dst (Dst_p). At storm onset (1128 UT), a large increase of the solar wind pressure caused the Dst index to increase. The same trend can be seen in Dst_p, although it did not become

18

positive; this difference is due to the fact that the intensity of the predicted ring current field was slightly greater than the observed one.

The ssc was immediately followed by a rectangular wave-like increase of ϵ, lasting for about 8 h. One can easily see that the predicted Dst variation (Dst_p) is quite similar to the observed one, in terms of not only the magnitude of the decrease, but also the time development. The ring current field developed rapidly until about the time when the rectangular change subsided and then decayed slowly. A slight irregularity in the decay was associated with minor substorm activity on 17 and 18 March. The AE index variation during the storm consisted of a main pulse associated with the rectangular wave-like change of ϵ and smaller increases before and after it. The main pulse was reasonably well reproduced, but the two smaller changes were exaggerated a little in the predicted AE index (AE_p).

2.1 Storm with an insignificant main phase

In this type of storm, a significant main phase fails to develop, in spite of a distinct ssc and the initial phase. The Dst index in Figure 6 shows that the storm of 13-15 February 1973 is of this type. It is easy to see that this particular solar wind flow contained only a small amount of ϵ. The predicted Dst variation is quite similar to the observed one. If the baseline can be adjusted for an increase of the observed Dst at about 20 UT on 13 February, the agreement between Dst and Dst_p can become even better.

2.2 Mini-storm

This type of storm develops as a result of a very intense impact of the storm (causing an unusually large ssc), but the main phase is weak and its duration is short (against the expectation from the magnitude of ssc). Figure 7 shows an example of such storms. The intense impact of the solar wind can
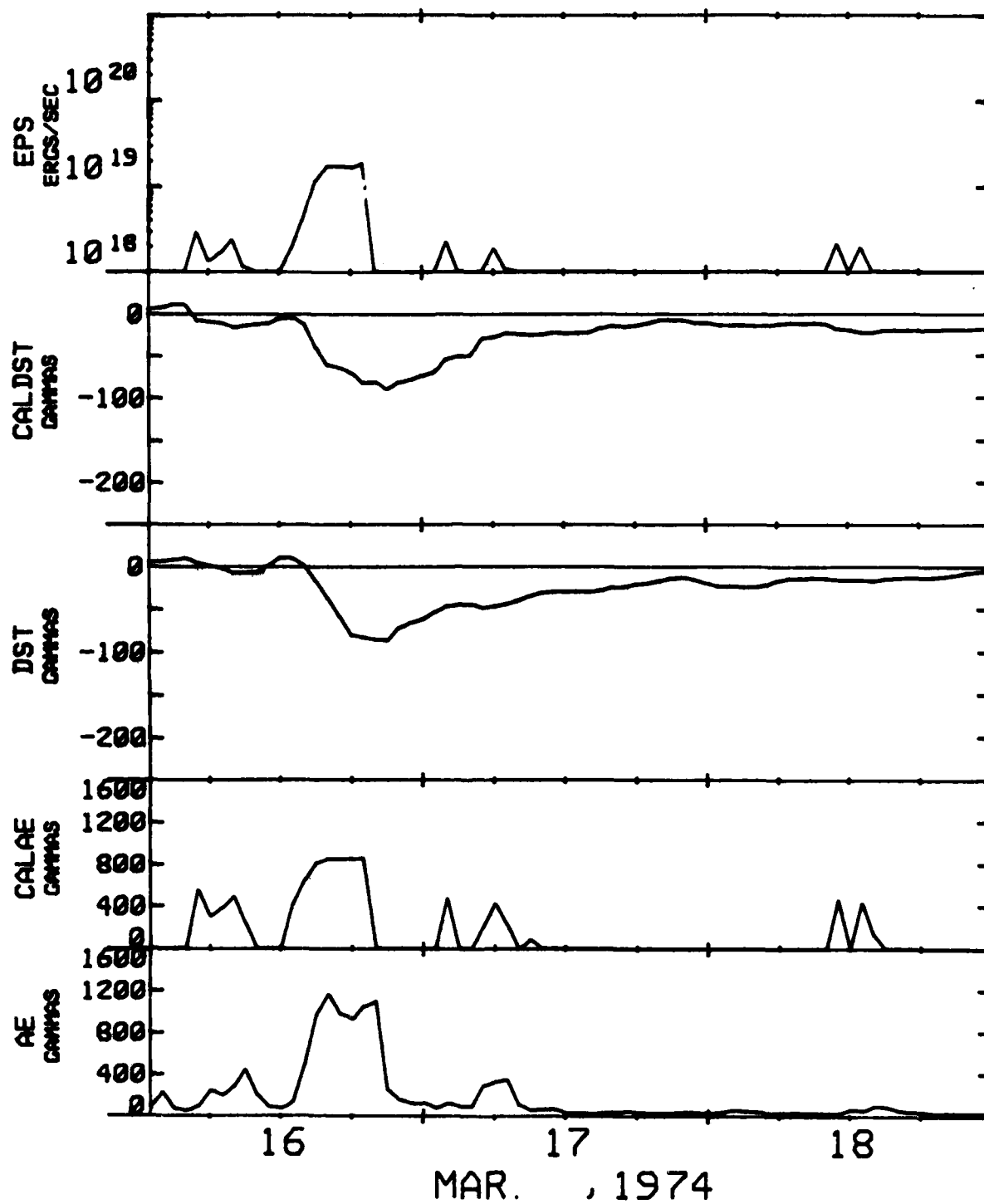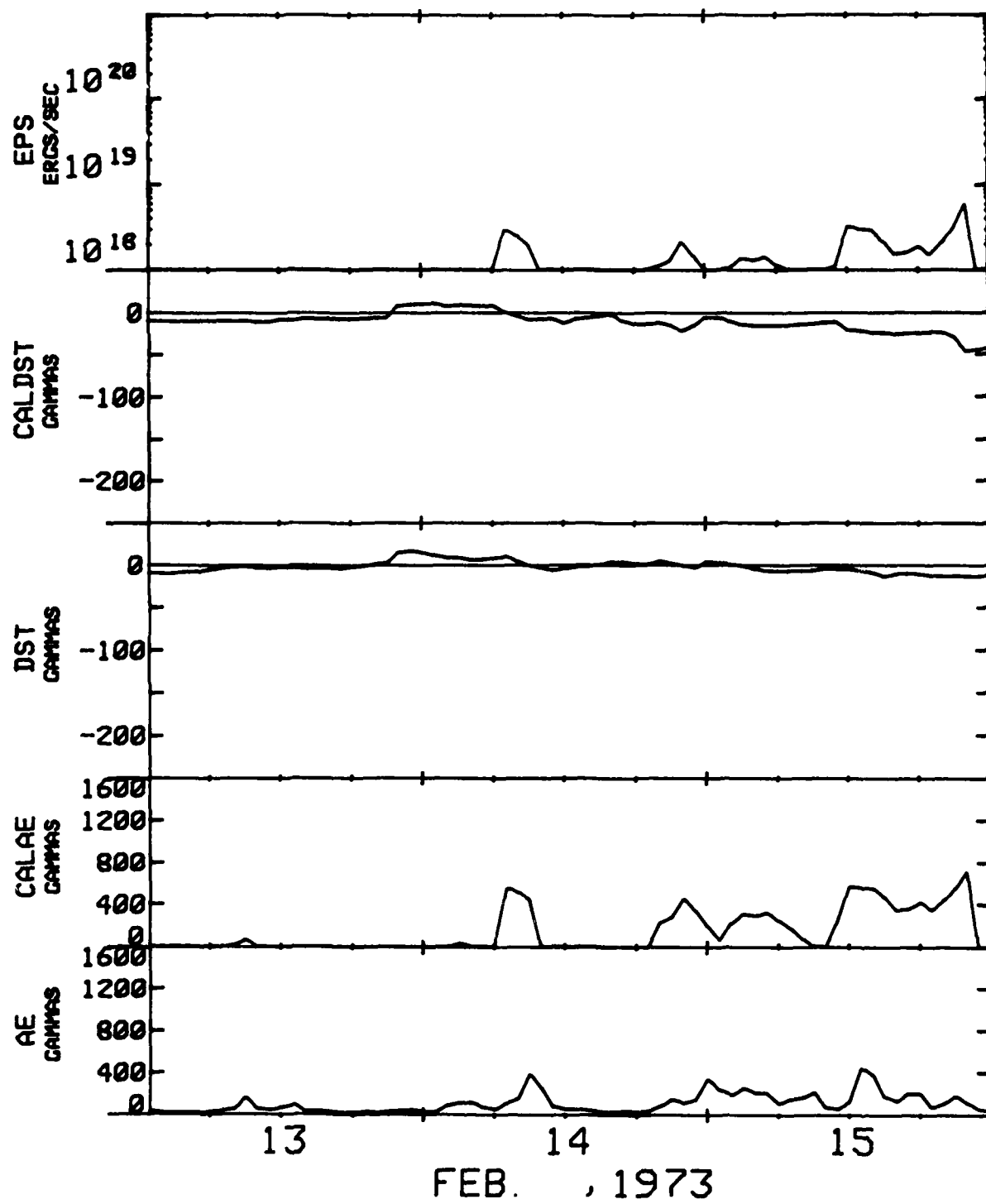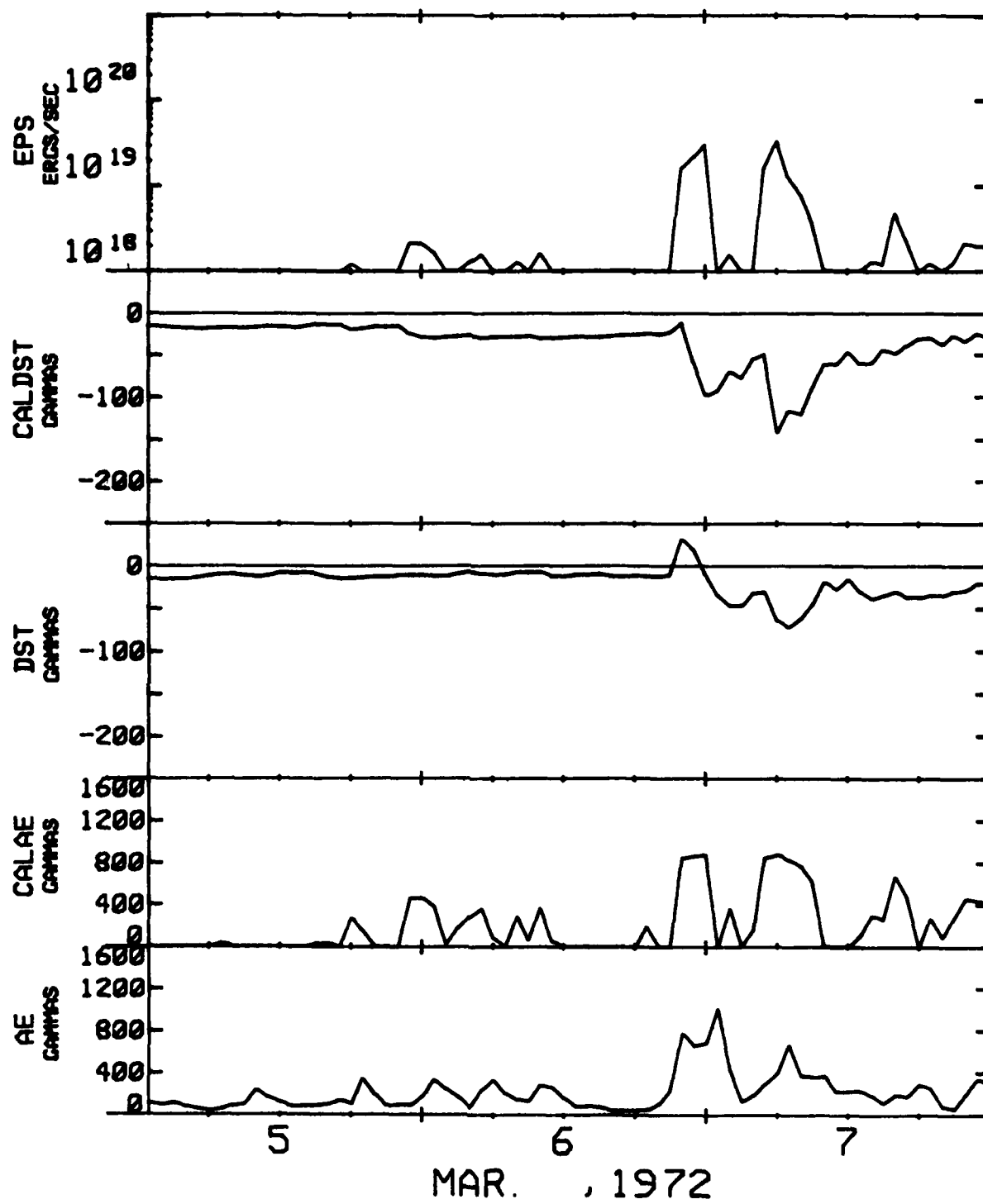
19

Fig. 5

20

Fig. 6

21

Fig. 7

22

clearly be recognized by a large ssc. One can easily recognize that complicated time variations of the observed Dst are fairly well reproduced by Dst_p. The difference between the observed Dst and Dst_p prior to storm onset is due to the fact that the substorm activity from ~ 22 UT 5 March to 06 UT 6 March caused an appreciable depression of Dst_p, but this depression was not registered in the observed Dst.

2.3 Typical storms

In Figures 8 and 9 we examine typical storms. The storm of 7-8 February 1967 began with a rapid increase of ε at the time of ssc. The main phase developed rapidly for about 10 h and began to decay near the end of 7 February as ε decreased. The increase of ε at about 06 UT on 8 February caused a new intensification of the main phase. One can clearly see that the development and decay of the main phase decrease is fairly well reproduced by the predicted Dst. The AE index is also fairly well reproduced.

In Figure 9, the storm of 31 March - 2 April 1973 began with a medium increase of ε at about 15 UT on 31 March, which caused a weak main phase. This increase of ε ended at about 22 UT on the same day. Another increase of ε ended at about 23 UT, but its magnitude was less than 10^{19} ergs^{-1} until about 12 UT on 1 April. As a result, the Dst decrease remained almost constant for more than 12 h. A new increase of ε began at about 09 UT on 1 April. An intense ring current belt began to develop when ε reached ~ 10^{19} ergs^{-1}. The main phase began to decay near the end of 1 April. Again, the overall pattern of the development of the main phase decrease is well reproduced by Dst_p. The predicted AE index agrees also fairly well with the observed one. However, during the period when the main phase was rapidly developing the observed AE index decreased.
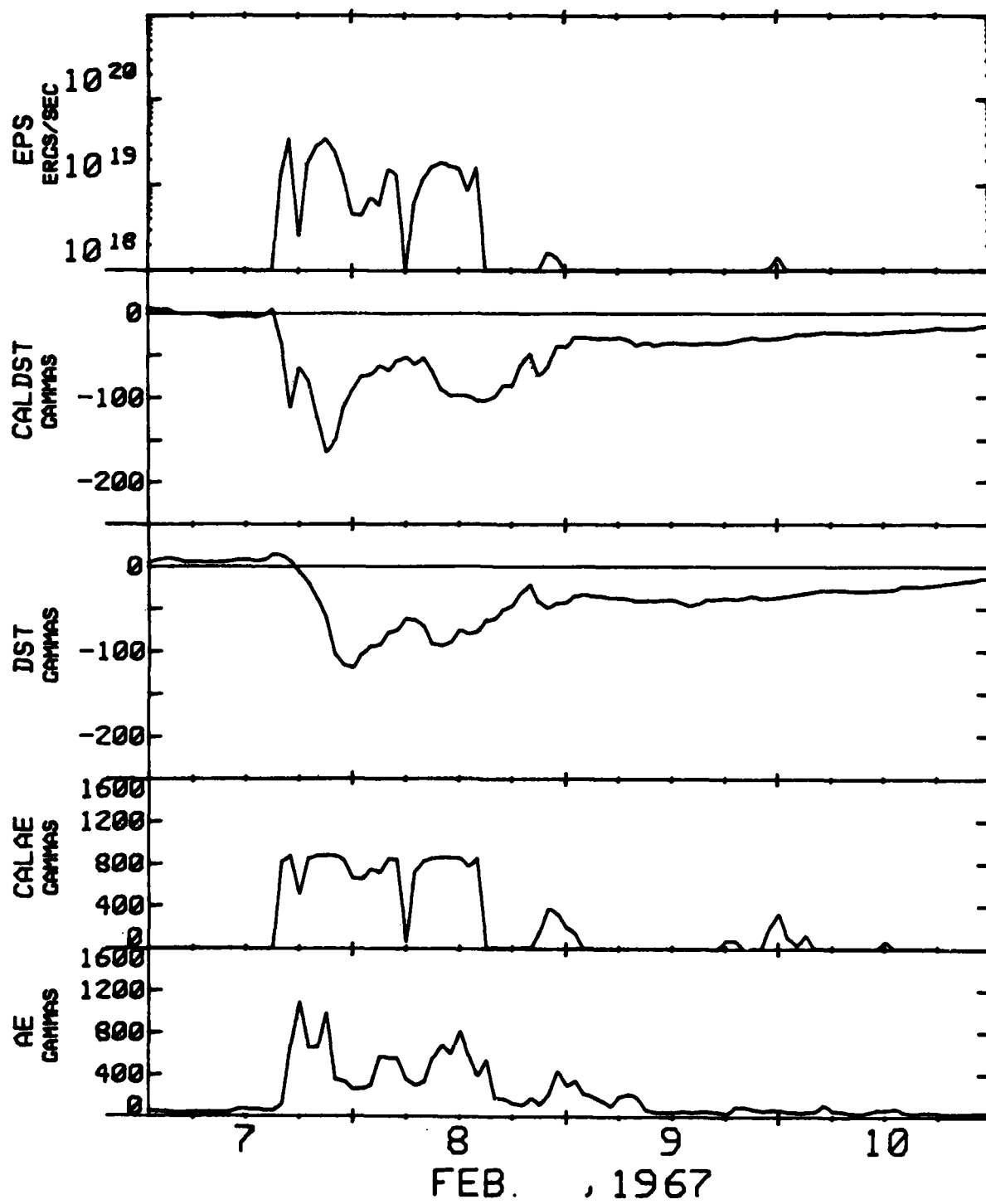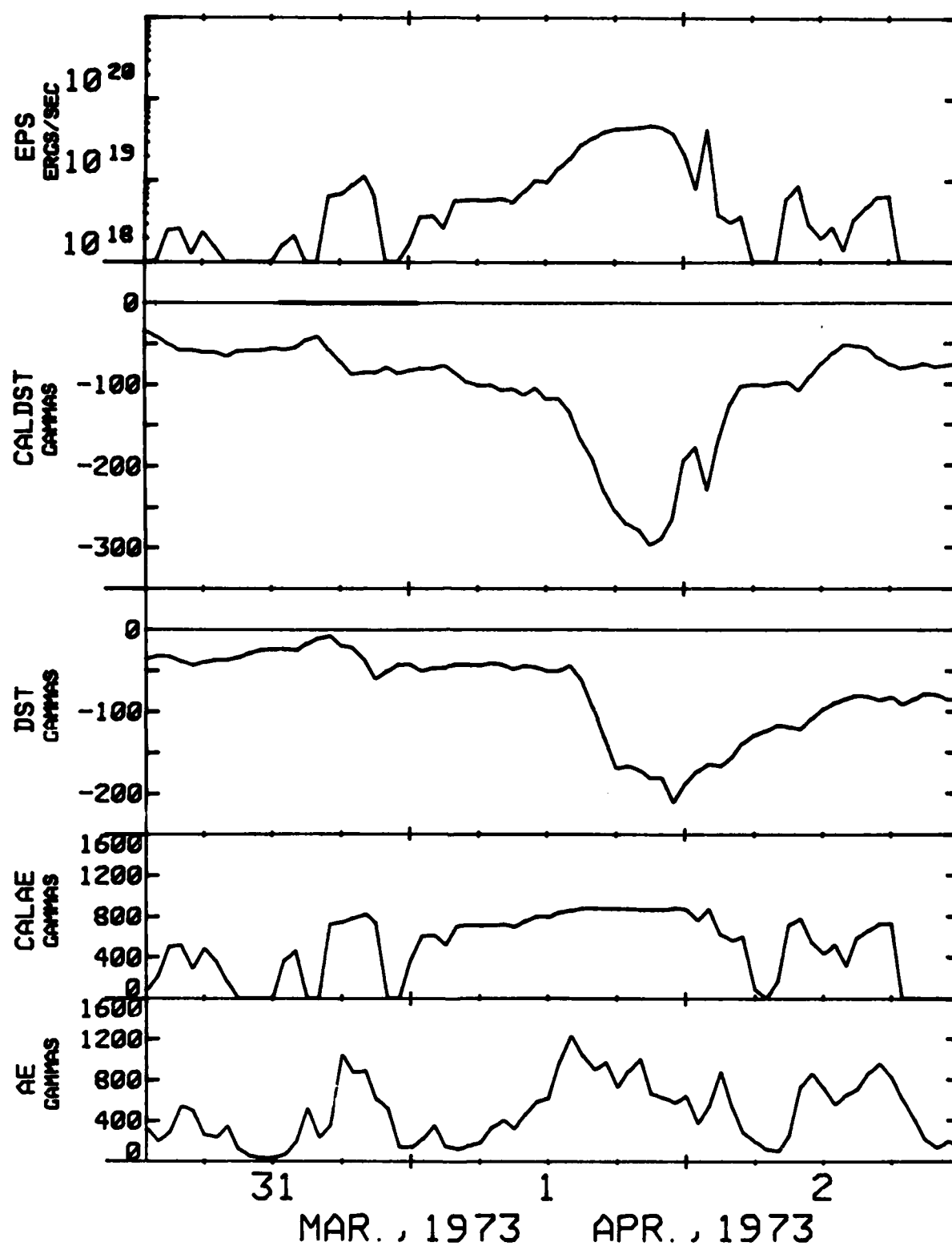
23

Fig. 8

24

Fig. 9

25

Figure 10 shows an example in which the predicted Dst was much greater than the observed Dst, although the overall feature of the time development was fairly well reproduced. In this storm of 15-18 February, 1967, ε reached one of the highest values during the last 15 years. There are at least two reasons for this discrepancy between the observed and predicted Dst variations. The first is that τ_R would have become less than 1 h for $\varepsilon > 5 \times 10^{19}$ ergs^{-1} or that ε would have been overestimated by assuming that ℓ_0 is a constant. A large increase of the solar wind pressure could have significantly reduced ℓ_0.

2.4 Long-lasting storms

Medium intensity storms last for about 48 h or so and decay slowly. Such storms are associated with a long-lasting increase of ε, with rapid changes, although the maximum magnitudes of ε remain less than 10^{19} ergs^{-1}. Figure 11 shows an example of such a storm. Unlike some of the major storms which develop rapidly and decay rapidly as well, this particular storm was characterized by a long-lasting Dst decrease, although the magnitude of the Dst values was not very large. Again, the predicted Dst reproduces fairly well the overall features of this type of storm.

3. Conclusion

We have demonstrated that one can make a fairly accurate prediction of the time development of the main phase decrease as manifested in the two geomagnetic indices Dst and AE, by monitoring $\varepsilon(t)$ upstream of the solar wind. Satellite ISEE/C, anchored at the libration point (at a distance of about 1.6×10^6 km toward upstream of the solar wind), can provide us with the necessary information to allow for a 1 h lead-time forecasting. A longer lead time forecasting would require numerical forecasting of ε in a way similar to
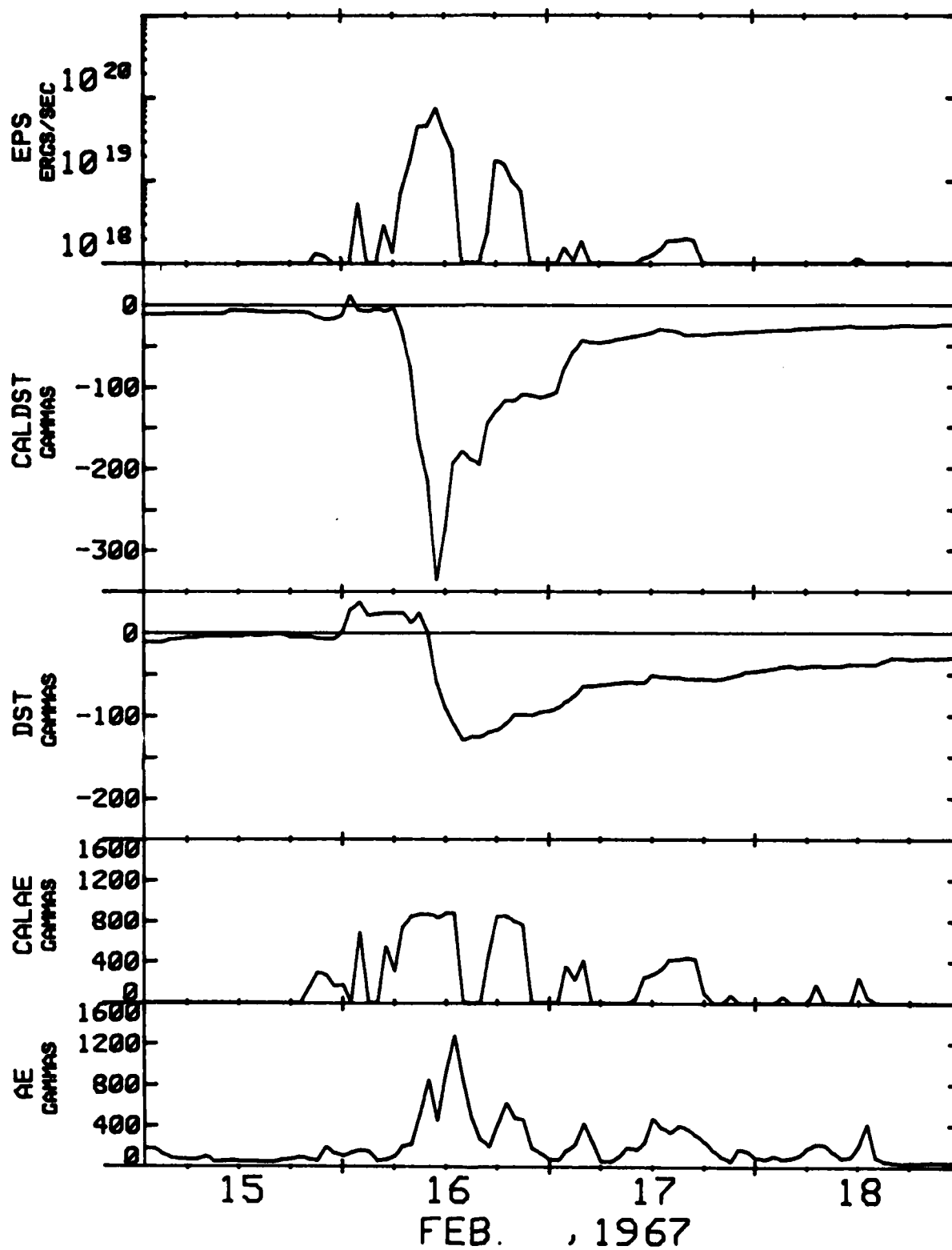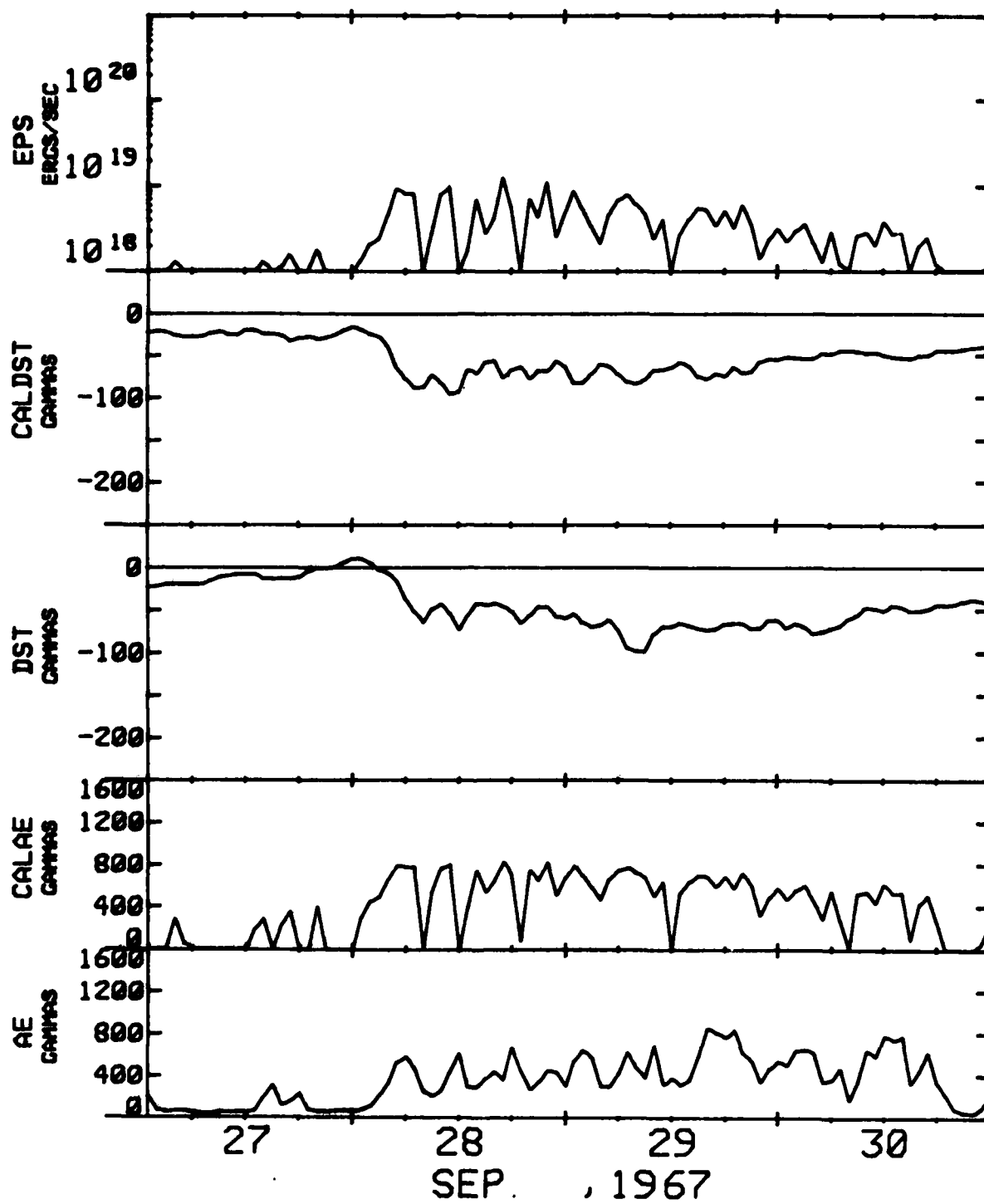
Fig. 10

27

Fig. 11

28

numerical weather forecasting. For this purpose, one must be able to simulate solar wind disturbances to determine V and B as a function of location and time in interplanetary space, and computed ε at the location of the earth.

V. Dependence of the geometry of the region of open field lines on the interplanetary magnetic field

Summary

In this section, we explain how the auroral oval geometry code has been developed. In particular, the geometry of the open flux area in the polar region is computed by superposing a uniform interplanetary magnetic field (IMF) with various orientation angles to a model of the magnetosphere. For details of this study, see Akasofu et al. (1981). The results show that the IMF B_y component is as important as the B_z component in "opening" the magnetosphere. It is also shown that the computed area of open field lines is remarkably similar to the observed ones which were determined by using the entry of solar electrons. In particular, when the IMF vector is confined in the X-Z plane and the B_z component has a large positive value, the open area becomes crescent-shaped, coinciding approximately with the cusp region.

1. Introduction

There are now several observations which indicate or suggest that drastic changes of the geometry of the open region occur as the orientation of the interplanetary magnetic field (IMF) vector changes. These observations are based on the geometry of the area into which low-energy or high-energy solar electrons enter. Here, we examine specifically the dependence of the geometry of the open field line region of the magnetosphere on the IMF by assuming a

simple linear superposition of the IMF on a model magnetospheric field. This study can also be considered to be a qualitative test of the validity of the superposition method, since one can compare the observed open region and the computed open region. It is indeed of great interest to examine whether or not this simple method can provide, as a first approximation, a topologically correct configuration of the open magnetosphere, without using a full-scale plasma simulation method.

In order to make the open region of the model as realistic as possible, one must carefully construct a three-dimensional model of the magnetosphere so as to be able to determine whether or not individual magnetospheric field lines are connected to the IMF field lines. Our model of the magnetosphere consists of the earth's dipole field (of magnetic moment M_E) and an image dipole field corresponding to a dipole of moment $7.0 \ M_E$ at $X = 28.0 \ R_E$, plus the magnetic field of the magnetotail (solar-magnetospheric coordinates are used in this paper). The tail field is simulated with two sets of 77 ring currents, one set in each hemisphere, separated by $0.2 \ R_E$ across the equatorial plane (the so-called "neutral sheet"). The currents flow counterclockwise (as viewed from the earth) in the northern ring and clockwise in the southern ring. They are distributed uniformly over a distance of 180 R_E, the nearest pair being located at $X = -10 \ R_E$; thus the successive rings are spaced uniformly by a distance of 2.37 R_E. In order to generate the observed 8° flaring of the tail, the radius of the rings is made to increase linearly by 14%. Further, the current intensity in successive rings is made to decrease with distance down the tail, starting with 250,000 A at $X = -10.0 \ R_E$ to zero at $X = -190 \ R_E$.

In this way, we construct first a model of the magnetosphere in the absence of the IMF and determine the geometry of the magnetopause. The

magnetopause consists of the magnetic field lines which "pass" through a very small area around the dayside neutral points (one in each hemisphere). Then, superposing the IMF of magnitude $|B| = 10\gamma$ in the model, we trace systematically a large number of field lines in the magnetosphere. Following Saunders (1976), the open field lines are defined as magnetic field lines which reach the magnetopause. The use of a relatively large value of $|B| = 10\gamma$ as the magnitude of the IMF is to examine effects of the IMF for the magnetosphere with a relatively short tail of length 200 R_E. It is generally accepted that the length of the tail is significantly longer than 200 R_E, so that a smaller magnitude of the IMF will have the same effects.

2.   Results and comparison with observations

The geometry of the open field line area is determined for two sets of IMF orientations. In the first set, the IMF vector is confined in the X-Z plane, and the angle between the Z-axis and the IMF vector is denoted by α, being reckoned positive as the vector rotates away from the Sun. The values of α examined here are 30°, 60°, 90°, 120° and 180°, so that the B_x component is always negative. In the second set, the IMF vector is confined in the Y-Z plane, and the angle between the Z-axis and the IMF vcector is denoted by β, being reckoned positive as the vector rotates toward the dawn side, so that the B_y component is always negative. The values of β examined here are also 30°, 60°, 90°, 120° and 180°.

(a) $\alpha = 30°$ ($B_x = -5.0\gamma$, $B_y = 0\gamma$, $B_z = 8.7\gamma$)

$\beta = 30°$ ($B_x = 0\gamma$, $B_y = -5.0\gamma$, $B_z = 8.7\gamma$).

Figure 12 shows the geometry of the northern open region for both sets of IMF orientations, $\alpha = 30°$ and $\beta = 30°$ in latitude-magnetic local time (MLT) coordinates. For $\alpha = 30°$, the open region is a very small area which is
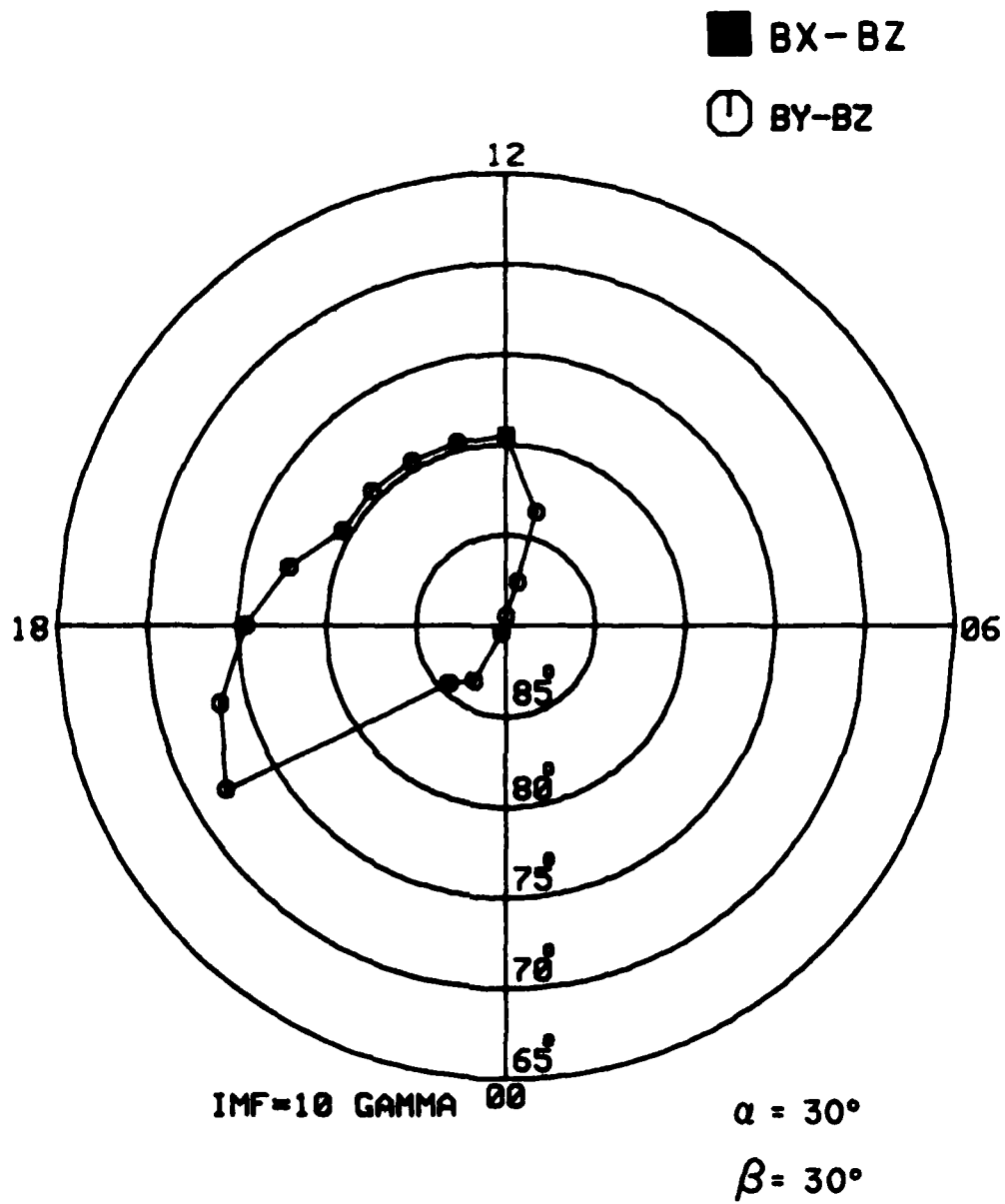
Fig. 12

32

located at 79° in latitude along the noon meridian. Therefore, the magneto-sphere is practically closed in this situation.

For β = 30°, the open region is almost confined in the evening sector in the northern hemisphere. Though it is not shown here, the open region is located in the morning sector in the southern hemisphere and its geometry is the mirror image (with respect to the noon-midnight meridian) of the northern one. The significance of this result will be discussed in (b).

(b) α = 60° (B_x = -8.7γ, B_y = 0γ, B_z = 5.0γ)

β = 60° (B_x = 0γ, B_y = -8.7γ, B_z = 5.0γ).

Figure 13 shows the geometry of the northern open region for both A = 60° and B = 60°. One can immediately recognize a large difference of the geometry of the open region for the same value (60°) of α and β.

For α = 60°, the magnetic field lines from a crescent-shaped region in the dayside can reach the magnetopause. It is interesting to note in this respect that McDiarmid et al. (1980) found that high-energy solar electron fluxes have a single peak in their pitch-angle distribution in a crescent-shaped area in the polar region and a double peak in the rest of the polar region when the IMF components were $B_x \sim$ -20γ, $B_y \sim$ -5γ and $B_z \sim$ +30γ. They suggested that the open region had a crescent shape. Their figures are reproduced here as Figures 14(a) and (b). One can see the similarity of the open regions in Figure 14(a) and Figure 13 (α = 60°). It is interesting to note also in this connection that the dayside auroral arc system lies in a crescent region similar to those shown in Figures 13 and 14(a) and remains bright even when the IMF B_z component is large and positive (although the nightside arc system becomes very faint).

For β = 60°, the open region is mainly confined to the evening sector in the northern hemisphere; in the southern hemisphere, the open region is mainly
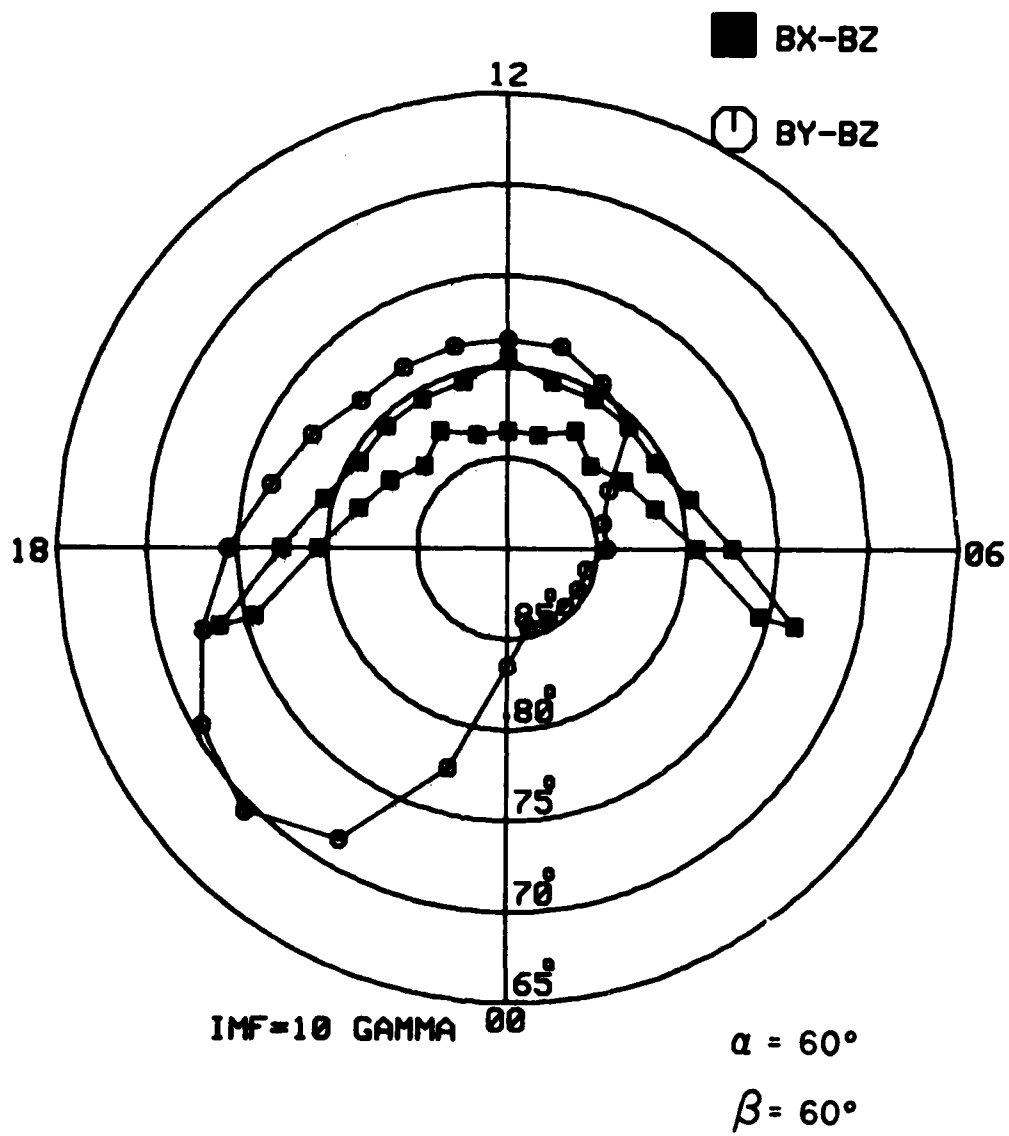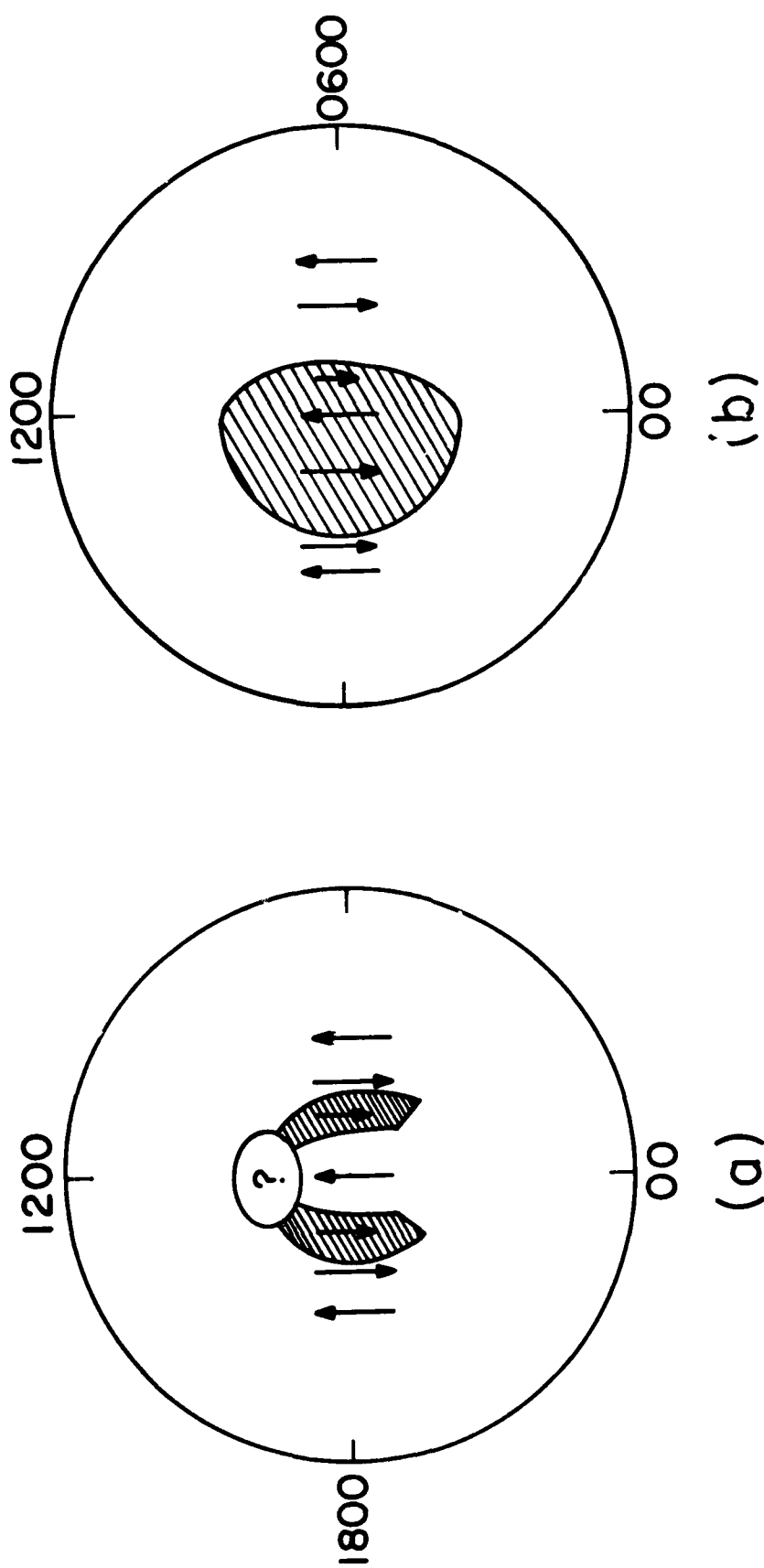
33

Fig. 15

IMF=10 GAMMA

BX-BZ

BY-BZ

$\alpha = 60°$

$\beta = 60°$

34

Fig. 14

35

confined to the morning sector. Again, the computed open region is similar to that suggested by McDiarmid et al. (1980), although the B_x component was greater than the B_y component, namely $B_x = 4.3\gamma$, $B_y = -0.7\gamma$ and $B_z = +9.2\gamma$. The open area in the southern hemisphere is the mirror image (with respect to the noon-midnight meridian) of it and appears in the morning sector, if the IMF vector is directed in the opposite direction, namely $B_x = 0\gamma$, $B_y = 8.7\gamma$ and $B_z = 5.0\gamma$. Such an asymmetry of the entry of solar electrons with respect to the sign of the IMF B_y component was noted by Meng et al. (1977). Further, Meng et al. (1977) showed that the situation is reversed in the southern hemisphere. Therefore, our results are qualitatively in agreement with the observations.

(c) $\alpha = 90°$ ($B_x = -10\gamma$, $B_y = 0\gamma$, $B_z = 0\gamma$)

$\beta = 90°$ ($B_x = 0\gamma$, $B_y = -10\gamma$, $B_z = 0\gamma$).

Figure 15 shows the results for $\alpha = 90°$ and $\beta = 90°$. The results for $\alpha = 90°$ are similar to those for $\alpha = 60°$, except that the open areas become appreciably greater than those for $\alpha = 60°$. It is thus of great interest to examine auroras under similar IMF conditions. Therefore, the nightside of the polar region is still essentially closed even for $\alpha = 90°$. For $\beta = 90°$, however, the open area expands drastically and becomes similar to that enclosed by the average size auroral oval. This result indicates that the B_y component is very important in making the nightside of the polar region open. For IMF polar angles of less than 90° or $B_z > 0$, the importance of the B_y component in opening the magnetosphere is indeed very crucial.

(d) $\alpha = 120°$ ($B_x = -8.7\gamma$, $B_y = 0\gamma$, $B_z = -5.0\gamma$)

$\beta = 120°$ ($B_x = 0\gamma$, $B_y = -8.7\gamma$, $B_z = -5.0\gamma$)

Figure 16 shows results for $\alpha = 120°$ and $\beta = 120°$. For both cases, the open area is close to the region enclosed by the normal size oval. This is
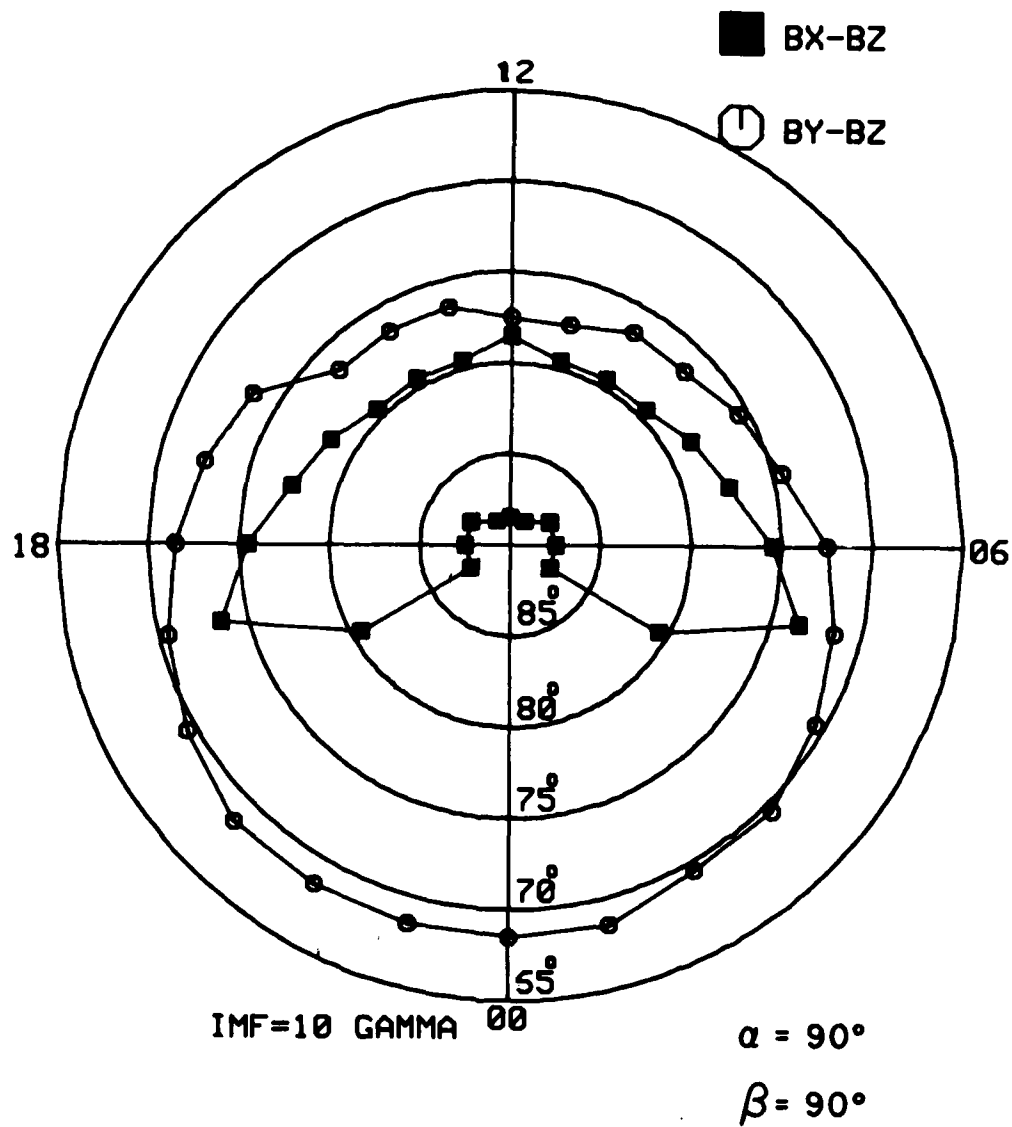
Fig. 15

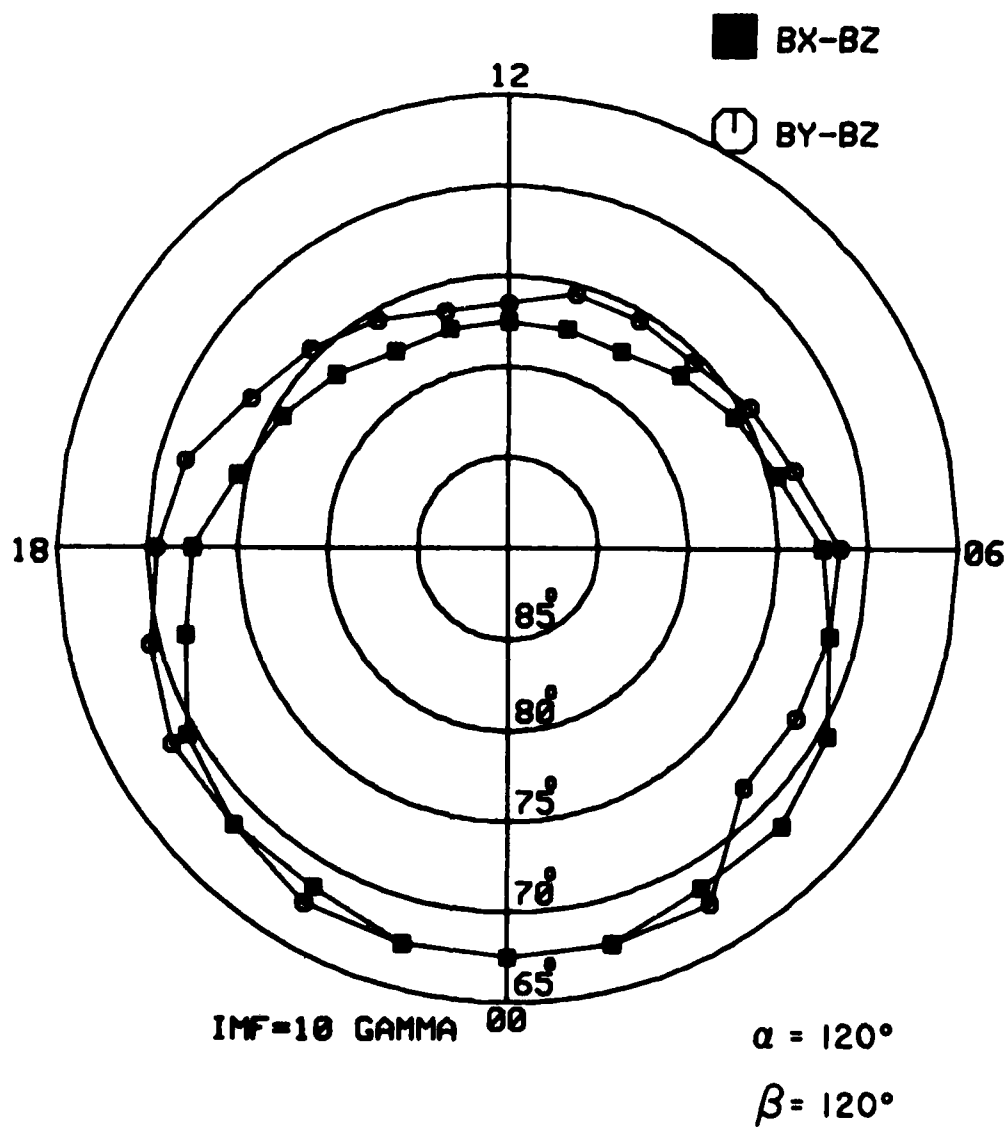IMF=10 GAMMA

α = 120°

β = 120°

Fig. 16

expected because the IMF B_z component is negative. Note that there is a slight asymmetry of the area with respect to the noon-midnight meridian for $\beta = 120°$.

(e) $\alpha = \beta = 180°$ ($B_x = 0\gamma$, $B_y = 0\gamma$, $B_z = -10\gamma$).

Figure 17 shows the result. The auroral oval is the same for both $\alpha = 180°$ and $\beta = 180°$. The open area is a little greater than that of the normal size oval.

3. Discussion

The remarkable similarity of the open regions (inferred from the impact area of solar electrons) by McDiarmid et al. (1980) and Meng et al. (1977) and the computed open regions proves the validity of the simple superposition method of the IMF on a magnetospheric field model, at least in studying the topological changes of the magnetospheric structure caused by variations of the orientation of the IMF.

VI. Polar cap arcs over Thule

The need for a computerized analysis of all-sky auroral photographs has been stressed during the last several years. Therefore, we have established a scheme to analyze all-sky photographs by using a digitizer and to display the location of auroral arcs on a geographic (or geomagnetic) map and in invariant latitude - MLT coordinates. The display is accomplished by specifying the geographic location of a fixed or moving observatory and the universal time (UT) when the photographs are taken as well as the type of camera used. The lens characteristics are digitized for the Fairchild lens, the University of Alaska all-sky (fish eye) camera and the IGY (mirror system) all-sky camera.
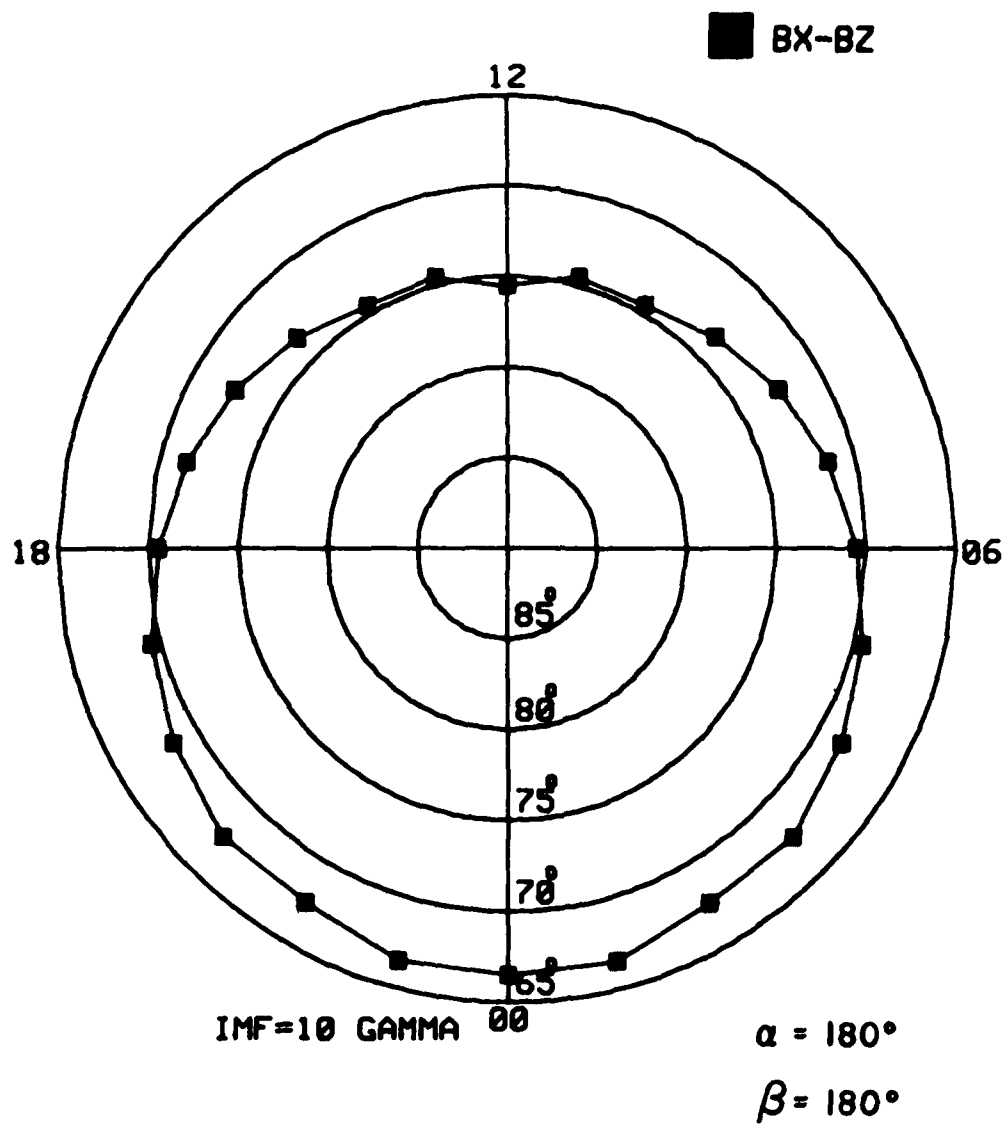
BX-BZ

12

18   06

85°

80°

75°

70°

65°

IMF=10 GAMMA   00

$\alpha = 180°$

$\beta = 180°$

Fig. 17

40

The scheme has been applied to all-sky photographs taken during the 1981 Thule expedition by the USAF Flying Observatory. Figure 18a shows some of the auroral photographs which were taken on January 21, 1981, showing a rapid development of a polar cap arc over Thule. Figure 18b shows the location of the arc in Figure 18a in invariant latitude - MLT coordinates.
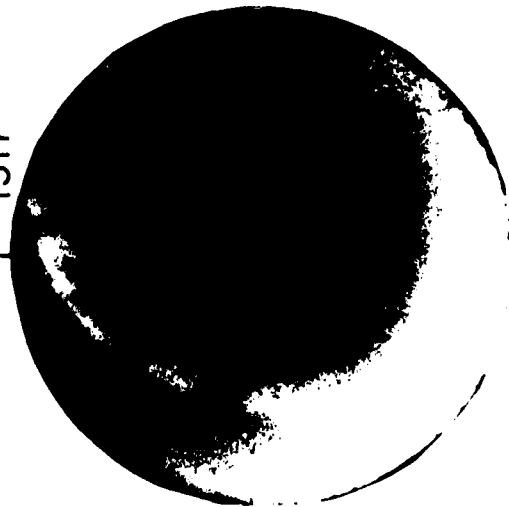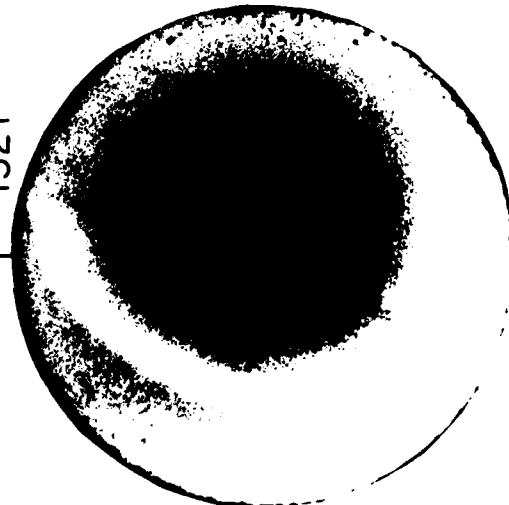
1315   1336 UT

1310   1321

Gg. NORTH
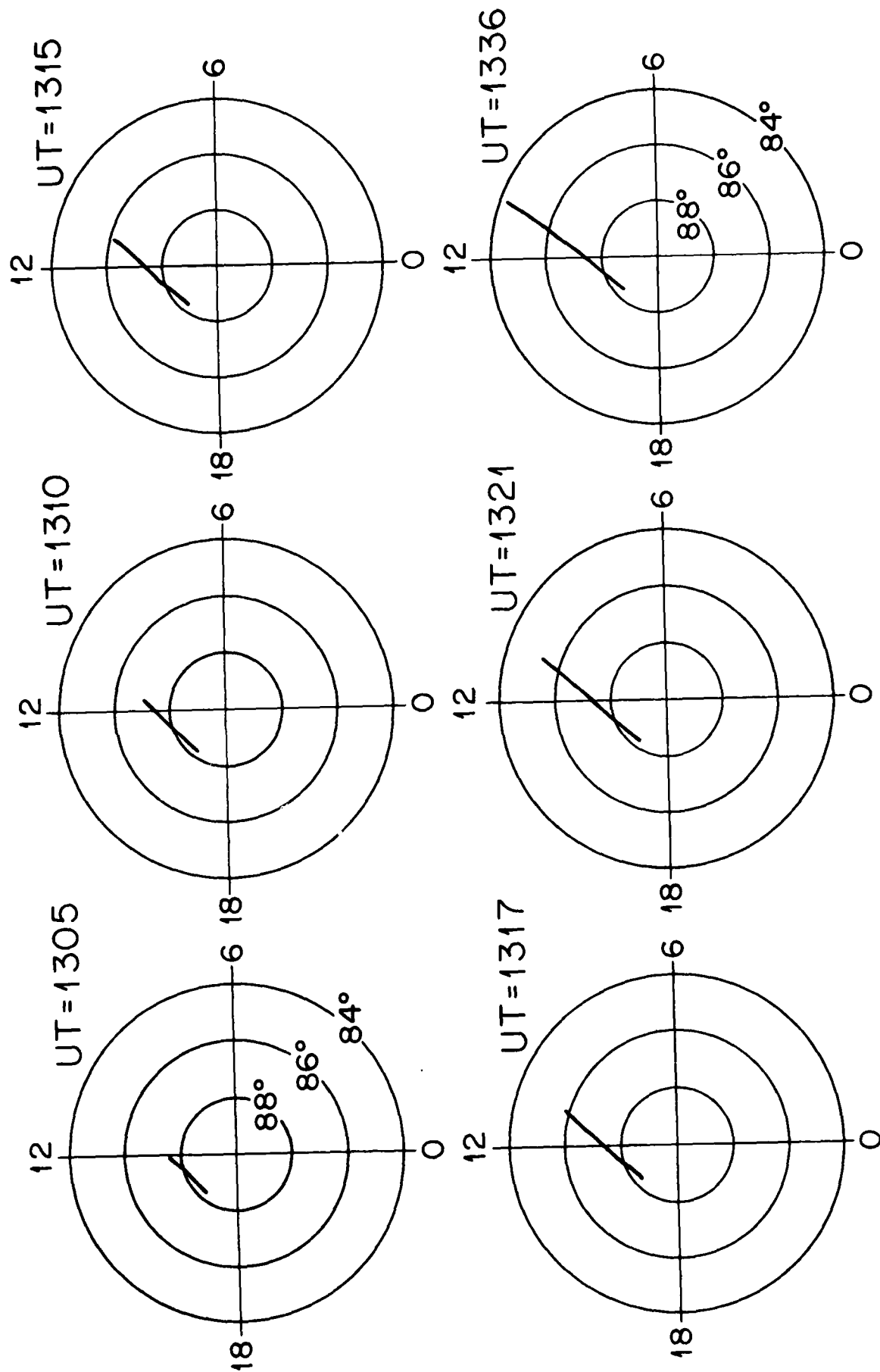1305   1317

JANUARY 21, 1981
THULE

Fig. 18a

42

Fig. 13b

43

References

Akasofu, S.-I., Energy coupling between the solar wind and the magnetosphere, Space Sci. Rev., 28, 121, 1981.

Akasofu, S.-I., Prediction of development of geomagnetic storms by using the solar wind-magnetosphere energy coupling function ϵ, Planet. Space Sci., 29, 1151, 1982.

Akasofu, S.-I., D. N. Covey, and C.-I. Meng, Dependence of the geometry of the region of open field lines on the interplanetary magnetic field, Planet. Space Sci., 29, 803, 1981.

Joselyn, J. A., and P. S. McIntosh, Disappearing solar filaments: A useful prediction of geomagnetic activity, J. Geophys. Res., 86, 4555, 1981.

McDiarmid, I. B., J. R. Burrows, and M. D. Wilson, Comparison of magnetic field perturbations and solar electron profiles in the polar cap, J. Geophys. Res., 85, 1163, 1980.

Meng, C.-I., S.-I. Akasofu, and K. A. Anderson, Dawn-dusk gradient of the precipitation of low energy electrons over the polar cap and its relation to the interplanetary magnetic field, J. Geophys. Res., 82, 5271, 1977.

Reiff, P. H., R. W. Spiro, and T. W. Hill, Dependence of polar cap potential drop on interplanetary parameters, J. Geophys. Res., 86, 7639, 1981.

Sojka, J. J., R. W. Schunk, and W. J. Raitt, Seasonal variations of the high latitude F region for strong convection, J. Geophys. Res., 87, 187, 1982.

Watkins, B. J., A numerical computer investigation of the polar F region ionosphere, Planet. Space Sci., 26, 559, 1978.

Whalen, J. A., Auroral oval plotter and monograph for determining corrected geomagnetic local time, latitude, and longitude for high latitudes in the northern hemisphere, Air Force Cambridge Res. Lab., AFCRL-70-0422, July 1970, Environmental Research Papers, No. 327.